Applications to Turbulence

21.1 GENERAL

Turbulence is a natural phenomenon in fluids that occurs when velocity gradients are high, resulting in disturbances in the flow domain as a function of space and time. Examples include smoke in the air, condensation of air on a wall, flows in a combustion chamber, ocean waves, stormy weather, atmospheres of planets, and interaction of the solar wind with magnetosphere, among others.

Although turbulence has been the subject of intensive study for the past century, it appears that many difficulties still remain unresolved, particularly in flows with high Mach numbers and high Reynolds numbers. Turbulent flows arise in contact with walls or in between two neighboring layers of different velocities. They result from unstable waves generated from laminar flows as the Reynolds number increases downstream. With velocity gradients increasing, the flow becomes rotational, leading to a vigorous stretching of vortex lines, which cannot be supported in two dimensions. Thus, turbulent flows are always physically three-dimensional, typical of random fluctuations. This makes 2-D simplifications unacceptable in most of the numerical simulation.

In turbulent flows, large and small scales of continuous energy spectrum, which are proportional to the size of eddy motions, are mixed. Here, eddies are overlapping in space, with large ones carrying small ones. In this process, the turbulent kinetic energy transfers from larger eddies to smaller ones, with the smallest eddies eventually dissipating into heat through molecular viscosity. In direct numerical simulation (DNS), a refined mesh is used so that all of these scales, large and small, are resolved. This is known as the deterministic method. Although some simple problems have been solved using DNS, it is not possible to undertake industrial problems of practical interest due to the prohibitive computer cost.

Since turbulence is characterized by random fluctuations, statistical methods rather than deterministic methods have been studied extensively in the past. In this approach, time averaging of variables is carried out in order to separate the mean quantities from fluctuations. This results in new unknown variable(s) appearing in the governing equations. Thus, additional equation(s) are introduced to close the system, the process known as turbulence modeling or Reynolds averaged Navier-Stokes (RANS) methods. In this approach, all large and small scales of turbulence are modeled so that mesh

refinements needed for DNS are not required. We discuss this topic in Sections 21.3 and 21.7.1.

A compromise between DNS and RANS is the large eddy simulation (LES) which has become very popular in recent years. Here, large-scale eddies are computed and small scales are modeled. Small-scale eddies are associated with the dissipation range of isotropic turbulence, in which modeling is simpler than in RANS. Since the large-scale turbulence is to be computed, the mesh refinements are required much more than in RANS, but not as much as in DNS because the small-scale turbulence is modeled. Governing equations and examples for LES are presented in Section 21.4 and Section 21.7.2.

Finally, we examine the physical aspects associated with DNS in Section 21.5, followed by numerical examples in Section 21.7.3.

21.2 GOVERNING EQUATIONS

Turbulent flowfields can be calculated with the Navier-Stokes system of equations averaged over space or time. When this averaging is performed, the equations describing the mean flowfield contain the averages of products of fluctuating velocities. In general, this will result in more unknowns than the number of equations available. Such difficulty can be resolved by turbulence modeling with additional equations being provided to match the number of unknowns. Such models are designed to approximate the physical behavior of turbulence. There are numerous ways of averaging flow variables: time averages, ensemble averages, spatial averages, and mass averages.

Time Averages

Any variable f is assumed to be the sum of its mean quantity $\overline{f}$ and its fluctuation part f',

$$f(x,t) = \overline{f}(x,t) + f'(x,t) \tag{21.2.1}$$

where $\overline{f}$ is the time average of f,

$$\overline{f}(x,t) = \frac{1}{\Delta t} \int_{t}^{t+\Delta t} f(x,t) dt \tag{21.2.2}$$

with

$$\overline{f'} = \frac{1}{\Delta t} \int_{t}^{t+\Delta t} f' dt = 0 \tag{21.2.3a}$$

The time average of the product of fluctuation parts of two different variables f' and g' is given by

$$\overline{f'g'} = \frac{1}{\Delta t} \int_{t}^{t+\Delta t} f' g' dt \neq 0 \tag{21.2.3b}$$

Here, the time interval Δt is chosen compatible with the time scale of the turbulent fluctuations, not only for the variable f but also for other variables within the physical domain.

Ensemble Averages

In terms of measurements of N identical experiments, $f(x, t) = f_n(x, t)$, we may determine the average,

$$\overline{f}(x, t) = \lim_{N \to \infty} \frac{1}{N} \sum_{n=1}^{N} f_n(x, t) \tag{21.2.4}$$

Spatial Averages

When the flow variable is uniform on the average such as in homogeneous turbulence, we may choose to use a spatial average defined as

$$\overline{f}(t) = \lim_{\Omega \to \infty} \frac{1}{\Omega} \int_{\Omega} f(x, t) d\Omega \tag{21.2.5}$$

Mass (Favre) Averages

For compressible flows, it is often more convenient to use mass (Favre) averages instead of time averages,

$$f = \tilde{f} + f'' \tag{21.2.6}$$

where the mean quantity $\tilde{f}$ is defined as

$$\tilde{f} = \frac{\overline{\rho f}}{\overline{\rho}} = \overline{f} + \frac{\overline{\rho' f'}}{\overline{\rho}} \tag{21.2.7}$$

and the fluctuation f'' has the property

$$\overline{\rho f''} = 0 \tag{21.2.8a}$$

whereas

$$\overline{f''} = -\overline{\rho' f'}/\overline{\rho} \neq 0 \tag{21.2.8b}$$

for the case of a time average. It is clear that the correlation of density fluctuations, ρ', with the fluctuating quantity, f', gives rise to a nonzero mean Favre fluctuation field, $\overline{f''}$. Thus, it is seen that the Favre average makes the turbulent compressible flow equations simpler with their form resembling those of incompressible flows. Despite these simplifications, however, the density fluctuations or compressibility effects must still be resolved; only the mathematical simplifications are achieved through Favre averages.

With time averages for incompressible flows and mass averages for compressible flows, the conservation equations can be derived as follows:

Time-Averaged Incompressible Flows

Continuity

$$\overline{v}_{i,i} = 0 \tag{21.2.9a}$$

Momentum

$$\rho \frac{\partial \overline{v}_j}{\partial t} + \rho \overline{v}_{j,i} \overline{v}_i = -\overline{p}_{,j} + (\overline{\tau}_{ij} + \tau^*_{ij})_{,i}$$ (21.2.9b)

with

$$\overline{\tau}_{ij} = 2\mu \overline{d}_{ij}, \qquad \overline{d}_{ij} = \frac{1}{2}(\overline{v}_{i,j} + \overline{v}_{j,i}), \qquad \tau^*_{ij} = -\overline{\rho v'_i v'_j}$$

Energy

$$\frac{\partial \overline{T}}{\partial t} + \overline{v}_i \overline{T}_{,i} = -(\overline{q}_i - q^*_i)_{,i}$$ (21.2.9c)

with

$$\overline{q}_i = -\alpha \overline{T}_{,i} \qquad q^*_i = -\overline{v'_i T'}$$

Mass (Favre)-Averaged Compressible Flows

Continuity

$$\frac{\partial \overline{\rho}}{\partial t} + (\overline{\rho} \tilde{v}_i)_{,i} = 0$$ (21.2.10a)

Momentum

$$\frac{\partial}{\partial t}(\overline{\rho} \tilde{v}_j) + (\overline{\rho} \tilde{v}_i \tilde{v}_j)_{,i} = -\overline{p}_{,j} + (\overline{\tau}_{ij} + \tilde{\tau}^*_{ij})_{,i}$$ (21.2.10b)

with

$$\overline{\tau}_{ij} = 2\mu \left(\overline{d}_{ij} - \frac{1}{3} \overline{d}_{kk} \delta_{ij} \right), \qquad \tau^*_{ij} = -\overline{\rho v''_i v''_j}$$

Energy

$$\frac{\partial}{\partial t}(\overline{\rho} E) + [\overline{\rho} \tilde{v}_i H]_{,i} = -\left(\overline{q}_i + q^*_i - \overline{\tau_{ij} v''_j} + \frac{1}{2} \overline{\rho v''_i v''_j v''_j} \right)_{,i} + [(\overline{\tau}_{ij} + \tau^*_{ij}) \tilde{v}_j]_{,i}$$

(21.2.10c)

with

$$E = \tilde{\varepsilon} + \frac{1}{2} \tilde{v}_i \tilde{v}_i, \qquad H = \tilde{H} + \frac{1}{2} \tilde{v}_i \tilde{v}_i, \qquad q^*_i = -\overline{\rho v''_i H''},$$

For time averaged incompressible flows, $-\overline{\rho v'_i v'_j}$ in (21.2.9b) and $-\overline{v'_i T'}$ in (21.2.9c) are identified as the Reynolds (turbulent) stress and Reynolds (turbulent) heat flux, respectively. The counterparts for mass-averaged compressible flows are $-\overline{\rho v''_i v''_j}$ in (21.2.10b) and $-\overline{\rho v''_i H''}$ in (21.2.10c), respectively. If time averages are used for compressible flows, the Reynolds stress components would be much more complicated. For this reason, mass averages are preferred for compressible flows.

These Reynolds stress tensors and Reynolds heat flux vectors are additional unknown variables. Therefore, additional governing equations other than those given in (21.2.9) and (21.2.10) matching the same number of unknowns must be provided. This is the process known as the turbulence closure or turbulence modeling. We discuss this subject in the next section.

21.3 TURBULENCE MODELS

There are many options in providing the closure process: zero-equation (algebraic) models, one-equation models, two-equation models, second order closure (Reynolds stress) models, and algebraic stress models as applied to incompressible flows. They are presented in Sections 21.3.1 through 21.3.4 with the effects of compressibility in Section 21.3.5.

21.3.1 ZERO-EQUATION MODELS

The purpose of zero-equation models is to close the system without providing extra differential equations. This may be achieved by the classical method of Prandtl mixing length [Prandtl, 1925]. Recent and more popular models are those advanced by Cebeci and Smith [1974] or Baldwin and Lomax [1978]. These models provide the Reynolds (turbulent) stress in terms of eddy (turbulent) viscosity μ_T,

$$\tau_{ij}^* = -\overline{\rho v_i' v_j'} = 2\mu_T d_{ij} = \mu_T \left(\overline{v}_{i,j} + \overline{v}_{j,i} \right) \tag{21.3.1}$$

where μ_T is computed by various approaches as described below.

Prandtl's Mixing Length Model

Historically, this is the earliest model proposed by Prandtl [1925] which applies to 2-D boundary layer problems:

$$\mu_T = \rho \ell^2 \left| \frac{d\overline{u}}{dy} \right| \tag{21.3.2}$$

where the Prandtl mixing length ℓ is given by

$$\ell = \kappa y$$

with κ being the von Karman constant ($\kappa = 0.41$).

The turbulent shear stress for the incompressible boundary layer flow is given by

$$\tau^* = \mu_T \frac{d\overline{u}}{dy} = \rho \ell^2 \left(\frac{d\overline{u}}{dy} \right)^2 \tag{21.3.3}$$

Upon integration of the above expression and using the empirical constant of integration from experiments, it can be shown that

$$u^+ = \frac{1}{\kappa} \ln y^+ + 5.5 \tag{21.3.4}$$

with $u^+ = \overline{u}/u_*$ and $y^+ = yu_*/\nu$ being the nondimensional relative velocity and nondimensional relative distance, respectively. A part of the turbulent velocity profile, called the law of the wall as given by (21.3.4) is valid only to the relative distance of approximately $y^+ = 30$; below this is the buffer zone and viscous sublayer as shown in Figure 21.3.1. From experiments, the viscous sublayer is identified by the range where y^+ is approximately equal to u^+. A smooth curve connects between the points $y^+ = 5$ and $y^+ = 30$. For flows such as in pipes or flat plates, the log layer deviates (defect layer) significantly at $y^+ \cong 500$ and above.
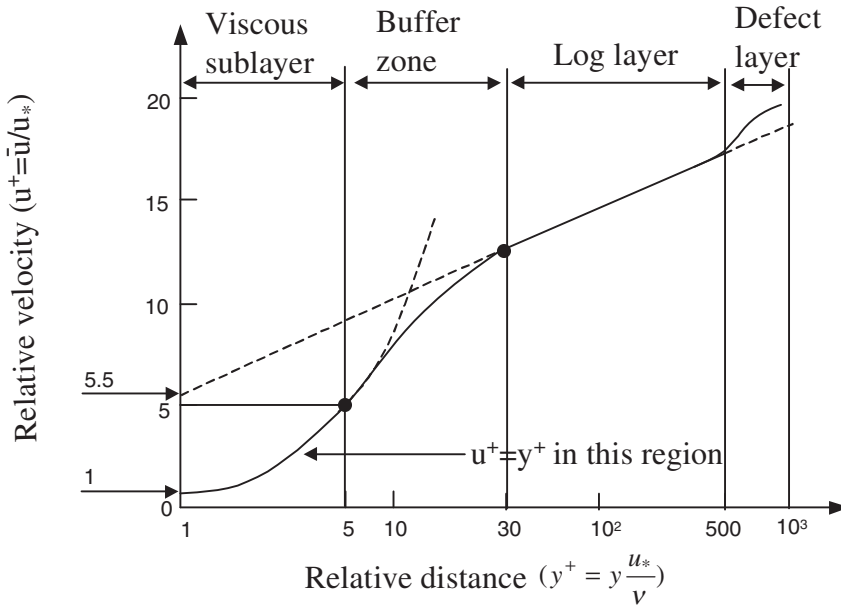
Figure 21.3.1 Two-dimensional turbulent boundary layer velocity profile showing various layers in terms of shear velocity $u_* = \sqrt{\tau/\rho}$.

Cebeci-Smith Model

The Cebeci-Smith model [1974] is designed for boundary layers consisting of inner layer region (Figure 21.3.2) with $\nu_T = \nu_T^{(I)}$ for $y < y_c$ and outer region with $\nu_T = \nu_T^{(o)}$ for $y > y_c$ where y_c is the critical height at which $\nu_T^{(I)}$ and $\nu_T^{(o)}$ coincide,

$$\nu_T^{(I)} = \rho\,\ell^2 |\nabla \times \overline{v}| \tag{21.3.5a}$$

$$\nu_T^{(o)} = 0.0168\rho\,\overline{u}_e\,\delta^* F \tag{21.3.5b}$$

Here ℓ is the Van Driest [1956] correction of the Prandtl mixing length,

$$\ell = \kappa y \lfloor 1 - \exp(-y^+/A^+) \rfloor \tag{21.3.6}$$

with

$$y^+ = y\frac{u_*}{\nu}, \qquad u_* = \sqrt{\frac{\tau_0}{\rho}}, \qquad A^+ = 26$$

τ_o = wall shear stress, $\overline{u}_e$ = external velocity at the boundary layer

δ^* = boundary layer displacement thickness.

$$F = \frac{1}{1 + 5.5\,(y/\delta)^6}$$

Here F denotes the intermittence at the edge of the boundary layer and δ is the boundary layer thickness.
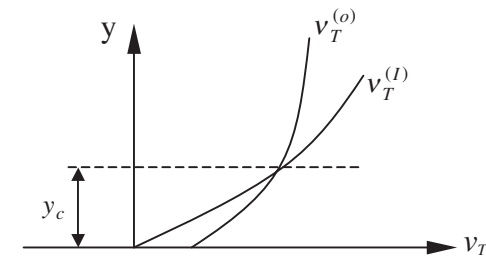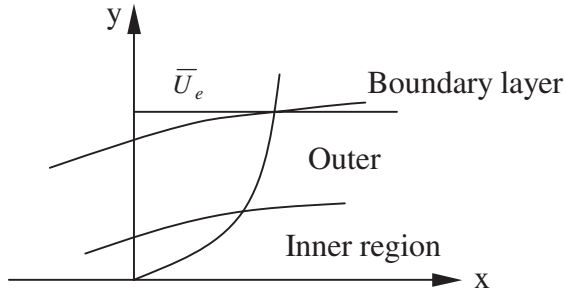
Figure 21.3.2 One-equation model [Cebeci-Smith, 1974; Baldwin-Lomax, 1978].

Baldwin-Lomax Model

The model given by (21.3.5) often encounters difficulties due to an uncertainty of the external velocity at the boundary layer $\overline{u}_e$ in (21.3.5b). To rectify this situation, Baldwin and Lomax [1978] proposed that the outer eddy viscosity be defined as

$$\nu_T^{(o)} = 0.0168\beta\, F y_{\max}\Gamma_{\max} \tag{21.3.7}$$

$$F = \frac{1}{1 + 5.5\,(\alpha y/y_{\max})^6}$$

$$\Gamma_{\max} = y\,[1 - \exp\,(-y^+/A)]\,|\nabla \times \overline{v}|$$

$$\alpha = 0.3, \qquad \beta = 1.6$$

For shear layer applications, only the outer eddy viscosity will apply. In general, the zero-equation models fail to perform well in the region of recirculation and separated flows.

Turbulent Heat Flux Vector

The unknown quantity in (21.2.9c) is the turbulent heat flux $q^*{}_i = -\overline{v'_i T'}$. This may be modeled as

$$q^*{}_i = \frac{\mu_T c_p}{\mathrm{Pr}_T}\overline{T}_{,i} \tag{21.3.8}$$

where Pr_T is the turbulent Prandtl number.

In the absence of thermoviscous dissipation, the governing equations (21.2.9a,b,c) together with any one of the turbulence models discussed above are closed. They can be solved simultaneously using suitable computational schemes of the previous chapters.

21.3.2   ONE-EQUATION MODELS

In the one-equation model, the eddy viscosity is defined as

$$\nu_T = c_\mu \ell \sqrt{K}, \quad c_\mu = 0.09$$

where K is the turbulent kinetic energy,

$$K = \frac{1}{2}\overline{v'_i v'_i}$$

Note that we have introduced one new variable K, so we must introduce one additional governing equation. This can be provided by the transport equation for the turbulence kinetic energy K,

$$\frac{DK}{Dt} = (\nu_k K_{,i})_{,i} + (\overline{\tau}_{ij}\overline{\mathbf{v}}_i)_{,j} \tag{21.3.9}$$

with

$$\nu_k = \nu + \nu_T$$

This turbulent kinetic energy transport equation (21.3.9) is added to the Navier-Stokes system of equations for simultaneous solution, with ν_T calculated as shown in Section 21.3.1.

21.3.3   TWO-EQUATION MODELS

K–ε Model

There are many two-equation models used in practice today. Among them is the K–ε model, which has been used most frequently for low-speed incompressible flows in isotropic turbulence. In this model, the turbulent stress tensor is given

$$\tau^*_{ij} = 2\mu_T \overline{d}_{ij} - \frac{2}{3}\overline{\rho}K\delta_{ij} \tag{21.3.10}$$

where the turbulent (eddy) viscosity μ_T is defined as

$$\mu_T = \overline{\rho}c_\mu \frac{K^2}{\varepsilon} \tag{21.3.11a}$$

with ε being the turbulent kinetic energy dissipation rate,

$$\varepsilon = \nu\overline{v'_{i,j}v'_{i,j}} \tag{21.3.11b}$$

Thus, the turbulent viscosity in (21.3.11a) contains two unknown variables, K and ε. It is therefore necessary that transport equations for K and ε be provided, which can be derived from the momentum equations. To obtain the turbulent kinetic energy transport equation, we take a time average of the product of the fluctuation component of the

velocity with the turbulent flow momentum equations. After some algebra, we arrive at

$$\overline{\rho}\frac{\partial K}{\partial t} + \overline{\rho}\overline{v}_i K_{,i} = A_{(k)} + B_{(k)} + C_{(k)} \tag{21.3.12a}$$

with $A_{(k)}, B_{(k)}, C_{(k)}$ denoting the production, dissipation, and diffusion transport, respectively,

$$A_{(k)} = \overline{\tau}_{ij}\overline{v}_{j,i}$$

$$B_{(k)} = -\rho\varepsilon$$

$$C_{(k)} = \left(\mu K_{,i} - \frac{1}{2}\overline{\rho}\overline{v_i' v_j' v_j'} - \overline{p'v_i'}\right)_{,i}$$

where the first, second, and third terms of C_k represent the molecular diffusion, turbulent diffusion, and pressure diffusion, respectively.

Similarly, the dissipation energy transport equation can be derived by taking a time average of the product of $2\nu v'_{i,j}$ with the derivative of momentum equations, resulting in

$$\overline{\rho}\frac{\partial \varepsilon}{\partial t} + \overline{\rho}\overline{v}_i\varepsilon_{,i} = A_{(\varepsilon)} + B_{(\varepsilon)} + C_{(\varepsilon)} \tag{21.3.12b}$$

with

$$A_{(\varepsilon)} = -2\mu(\overline{v'_{i,k}v'_{j,k}} + \overline{v'_{k,i}v'_{k,j}})\overline{v}_{i,j}$$

$$B_{(\varepsilon)} = -2\mu\overline{v'_k v'_{i,j}}\overline{v}_{i,jk} - 2\mu\overline{v'_{i,k}v'_{i,j}v'_{k,j}} - 2\mu\nu\overline{v'_{i,kj}v'_{i,kj}}$$

$$C_{(\varepsilon)} = (\mu\varepsilon_{,j} - \mu\overline{v'_j v'_{i,k}v'_{i,k}} - 2\mu\overline{p'_{,i}v'_{j,i}})_{,j}$$

which represent production of dissipation, dissipation of dissipation, and dissipation transport terms, respectively. Here, the first, second, and third terms of $C_{(\varepsilon)}$ indicate molecular dissipation, turbulent dissipation, and pressure dissipation, respectively.

As a consequence of (21.3.12a,b), we are now confronted with more unknowns than we originally started in (21.3.11a,b). To avoid such additional unknowns, Launder and Spalding [1972] proposed the so-called K–ε model in which the turbulent kinetic energy and dissipation energy transport equations can be written as follows:

$$\frac{\partial}{\partial t}(\overline{\rho}K) + (\overline{\rho}K\overline{v}_i)_{,i} = (\overline{\tau}_{ij}\overline{v}_j)_{,i} - \overline{\rho}\varepsilon + (\mu_k K_{,i})_{,i} \tag{21.3.13a}$$

$$\frac{\partial \overline{\rho}\varepsilon}{\partial t} + (\overline{\rho}\varepsilon\overline{v}_i)_{,i} = c_{\varepsilon 1}(\overline{\tau}_{ij}\overline{v}_j)_{,i} - c_{\varepsilon 2}\overline{\rho}\frac{\varepsilon^2}{K} + (\mu_\varepsilon\varepsilon_{,i})_{,i} \tag{21.3.13b}$$

with

$$\mu_\kappa = \mu + \frac{\mu_T}{\sigma_\kappa}, \qquad \mu_\varepsilon = \mu + \frac{\mu_T}{\sigma_\varepsilon}$$

$$c_\mu = 0.09, \quad c_{\varepsilon 1} = 1.45 \sim 1.55, \quad c_{\varepsilon 2} = 1.92 \sim 2.00, \quad \sigma_\kappa = 1, \quad \sigma_\varepsilon = 1.3 \tag{21.3.14}$$

Notice that the first, second, and third terms on the right-hand side of (21.3.13a,b) correspond to the production, dissipation, and transport terms, respectively, as defined in (21.3.12a,b). The closure constants given in (21.3.14) are obtained from the experimental

data. They may also be correlated (calibrated) by direct numerical simulation discussed in Section 21.5. It is seen that no new variables other than K and ε are contained in (21.3.13a,b). These two equations can now be combined in the solution of the Navier-Stokes system of equations.

Nonlinear (anisotropic) *K–ε* Model

An improved version of the K–ε model was proposed by Speziale [1987] in which the turbulent stress tensor includes the frame indifferent Oldroyd derivative.

$$\tau_{ij}^* = 2\mu_T \overline{d}_{ij} - \frac{2}{3}\overline{\rho} K\delta_{ij} + \hat{\tau}_{ij} \tag{21.3.15}$$

where $\hat{\tau}_{ij}$ represents the nonlinear anisotropic turbulence,

$$\hat{\tau}_{ij} = 4\overline{\rho} C_D c_\mu^2 \frac{K^3}{\varepsilon^2}\left(\hat{d}_{ij} - \frac{1}{3}\hat{d}_{kk}\delta_{ij} + \overline{d}_{ik}\overline{d}_{kj} - \frac{1}{3}\overline{d}_{ki}\overline{d}_{kj}\right)$$

$$\hat{d}_{ij} = \frac{\partial \overline{d}_{ij}}{\partial t} + \overline{v}_k \overline{d}_{ij,k} - d_{kj}\overline{v}_{i,k} - d_{ki}\overline{v}_{j,k}$$

with $C_D = 1.68$ as calibrated from the experimental data.

K–ω Model

The basic idea of the K–ω model was originated by Kolmogorov [1942] with turbulence associated with vorticity, ω, being proportional to K^2/ℓ,

$$\omega = c\frac{K^2}{\ell} \tag{21.3.16a}$$

where c is a constant. Thus, the eddy viscosity may be written as

$$\mu_T = \rho K/\omega \tag{21.3.16b}$$

The transport equations for k and ω [Wilcox, 1988] may be written as

$$\frac{\partial}{\partial t}(\overline{\rho} K) + (\overline{\rho} K \overline{v}_{,i})_{,i} = (\mu_k K_{,i})_{,i} + (\tau_{ij}\overline{v}_j)_{,i} - \beta^*\overline{\rho} K\omega \tag{21.3.17a}$$

$$\frac{\partial}{\partial t}(\overline{\rho}\omega) + (\overline{\rho}\omega\overline{v}_i)_{,i} = (\mu_\varepsilon \omega_{,i})_{,i} + \alpha\frac{\omega}{K}(\tau_{ij}\overline{v}_j)_{,i} - \beta\overline{\rho}\omega^2 \tag{21.3.17b}$$

with the closure constants,

$$\alpha = 5/9, \qquad \beta = 3/40, \qquad \beta^* = 9/100, \qquad \sigma = 1/2, \qquad \sigma^* = 1/2$$

Wall Functions

At the wall boundary, the velocity gradients are high, requiring excessive mesh refinements. In order to alleviate such excessive mesh refinements, the so-called wall function [Launder and Spalding, 1972] is needed. To this end, the boundary conditions for K and ε in the near wall regions may be specified as

$$K = \frac{|\tau_w|}{\sqrt{c_\mu}}, \quad \varepsilon = \frac{|\tau_w|}{a^\delta}$$

where the wall shear stress τ_w is given by

$$|\tau_w| = \frac{a|u_*|\left(c_\mu^{0.5}K\right)^{0.5}}{\ell_n(E\delta^+)} \tag{21.3.18}$$

with the turbulent kinetic energy K computed iteratively at a distance $\delta^+ \geq 12$, $a = 0.419$, $\varepsilon = 9.793$, and

$$\delta^+ = \mathrm{Re}\,\delta\left(c_\mu^{0.5}K\right)^{0.5}$$

For $\delta^+ < 12$ the laminar stress is given by

$$|\tau_w| = \frac{|u_*|}{\mathrm{Re}\,\delta} \tag{21.3.19}$$

where the viscosity in the near wall regions is estimated as

$$\mu_* = \mathrm{Re}\,\delta\frac{|\tau_w|}{|u_*|}$$

If the flow velocity increases, however, it has been observed that the role of the wall function becomes unrealistic and the K–ε model is considered unreliable. The K–ε model described here is based on isotropic turbulence and is referred to as standard K–ε model.

The following boundary conditions are typically imposed for a wall-bound turbulent flow:

(a) *Inflow*: specify $\overline{u}$, K, and ε
(b) *Outflow*: specify $\overline{v}$ by extrapolation, $\overline{u}$ by mass balance; $\overline{p}$, K, and ε by extrapolation
(c) Wall boundaries
  (i) Standard two-layer form of the law of the wall

$$u^+ = \frac{1}{\kappa}\ln y^+ + 5, \qquad \frac{K}{u_*^2} = c_\mu^{-\frac{1}{2}}, \qquad \varepsilon = c_\mu^{\frac{1}{2}}\frac{K^{\frac{3}{2}}}{\kappa y} \tag{21.3.20}$$

  These conditions are applied at the first grid point y away from the wall if $y^+ \equiv yu_*/v \geq 11.6$ with $u^+ = \overline{u}/u_*$. If $y^+ < 11.6$, then $\overline{u}$, K, and ε are interpolated to the wall values based on viscous sublayer constraints.
  (ii) Three-layer form of the law of the wall

$$u^+ = \begin{cases} y^+ & \text{for } \leq 5 \\ -3.05 + 5\ln y^+ & \text{for } 5 < y^+ \leq 30 \\ 5.5 + \dfrac{1}{\kappa}\ln y^+ & \text{for } y^+ > 30 \end{cases} \tag{21.3.21}$$

For the K–ω model, Wilcox [1989] proposes the wall function for ω in the form,

$$\omega = \frac{K^{1/2}}{c_\mu^{1/4}} \tag{21.3.22a}$$

and further argued that the pressure gradient must be included for high-pressure gradient flows.

$$\omega = \frac{u_*}{0.41 y \sqrt{c_\mu}} \left(1 - 0.32 \frac{y}{\rho \sqrt{u_*}} \frac{dp}{dx} \right) \tag{21.3.22b}$$

21.3.4   SECOND ORDER CLOSURE MODELS (REYNOLDS STRESS MODELS)

Effects of streamline curvature, sudden changes in strain rate, secondary motion, etc. can not be accommodated in the two equation models presented in Section 21.3.3. The second order closure models or Reynold stress models are designed to handle these features. The stress tensor is given by

$$\tau_{ij} = \overline{\tau}_{ij} + \tau_{ij}^*$$

with τ_{ij}^* being the Reynold stress

$$\tau_{ij}^* = -\rho \overline{v'_i v'}_j$$

The Reynolds stress transport equation is of the form

$$\frac{\partial \tau_{ij}^*}{\partial t} + (\overline{v}_k \tau_{ij}^*),_k = A_{ij} + B_{ij} + C_{ij} + D_{ij} \tag{21.3.23}$$

where A_{ij}, B_{ij}, C_{ij}, and D_{ij}, denote production, dissipation (destruction), diffusion, and pressure strain, respectively.

$$A_{ij} = -\tau_{ik}^* \overline{v}_{j,k} - \tau_{jk}^* \overline{v}_{i,k} \tag{21.3.24}$$

$$B_{ij} = -2\mu \overline{v'_{i,k} v'}_{j,k} \tag{21.3.25}$$

$$C_{ij} = \lfloor -\left(\rho \overline{v'_i v'_j v'_k} + \overline{p' v'_i} \delta_{jk} + \overline{p' v'_j} \delta_{ik} \right) + \mu \tau_{ij,k}^* \rfloor,_k \tag{21.3.26}$$

$$D_{ij} = \overline{p'(v'_{i,j} + v'_{j,i})} \tag{21.3.27}$$

Note that new variables are introduced in C_{ij} and D_{ij}, whereas A_{ij} and B_{ij} contain no new variables. Thus, we must model the diffusion transport and pressure-strain tensors. Although dissipation occurs at the smallest scales and one can use the Kolmogorov hypothesis of local isotropy, it may become anisotropic close to the wall, and thus modeling is needed. We discuss below some of the well-known second order closure models.

Dissipation Tensor

Since ε is the dissipation rate, this may be treated similarly as in the K–ε model. However, Hanjalic and Launder [1976] propose to add an extra term representing anisotropy close to the wall.

$$B_{ij} = -\frac{2}{3} \rho \varepsilon \delta_{ij} - 2 f \rho \varepsilon b_{ij} \tag{21.3.28}$$

where f is a damping function and b_{ij} denotes the dimensionless anisotropy tensor, respectively,

$$f = (1 + 0.1\,\mathrm{Re}^*)^{-1}, \quad \mathrm{Re}^* = K^2/(\varepsilon\nu)$$

$$b_{ij} = -\left(\frac{\tau_{ij}^* - \dfrac{2}{3}\rho K \delta_{ij}}{2\rho K} \right)$$

Diffusion Transport Tensor

The turbulence transport is characterized by the diffusion tensor C_{ijk}. Launder, Reece, and Rodi [1975] proposed that this tensor be modeled as

$$C_{ijk} = -\frac{2}{3}c\frac{K^2}{\varepsilon}(\tau_{ij,k}^* + \tau_{ik,j}^* + \tau_{jk,i}^*) + \mu\tau_{ij,k}^* \tag{21.3.29a}$$

with $c \cong 0.11$. They also postulated a more general form,

$$C_{ijk} = -c'\frac{K}{\rho\varepsilon}(\tau_{ij,m}^*\tau_{mk}^* + \tau_{ik,m}^*\tau_{mj}^* + \tau_{jk,m}^*\tau_{mi}^*) + \mu\tau_{ij,k}^* \tag{21.3.29b}$$

with $c' \cong 0.25$.

Pressure-Strain Correlation Tensor

This is an important contribution in turbulence since the terms involved in the pressure-strain tensor are of the same order of magnitude as the production terms. Pressure can be obtained by solving the pressure Poisson equation in which the forcing functions consist of slow and rapid fluctuations. To see this, we examine the pressure Poisson equation in the form,

$$p_{,ii} = -\rho(v_{i,j}v_j)_{,i} = -\rho(v_{i,ji}v_j + v_{i,j}v_{j,i})$$

In terms of mean and fluctuating components, we obtain

$$p'_{,ii} = -\rho(f_s + f_r) \tag{21.3.30}$$

where the slow forcing function f_s and rapid forcing function f_r are given by

$$f_s = \left(v_i'v_j' - \overline{v_i'v_j'}\right)_{,ij} \tag{21.3.31a}$$

$$f_r = 2\overline{v}_{i,j}v_{j,i}' \tag{21.3.31b}$$

The solution of (21.3.30) via Green functions results in integral forms corresponding to (21.3.31a) and (21.3.31b) such that the pressure-strain tensor can be written as

$$D_{ij} = E_{ij} + F_{ijkm}\overline{v}_{k,m} \tag{21.3.32}$$

where E_{ij} and $F_{ijkm}\overline{v}_{k,m}$ denote the slow pressure strain and rapid pressure strain, respectively. For inhomogeneous turbulence, the mean velocity present in the rapid pressure strain (21.3.31b) implies the process is not localized, leading to the argument that the single-point correlation may not be adequate. This would require that the products of fluctuating properties be correlated at two separate physical locations (two-point

correlation). This task is difficult, and the so-called *locally homogeneous approximation* may be adopted as described below.

Rotta [1951] postulated that the slow pressure strain is of the form

$$E_{ij} = c_1 \frac{\varepsilon}{K} \left(\tau_{ij}^* + \frac{2}{3} \rho K \delta_{ij} \right) \quad 1.4 \le c_1 \le 1.8 \tag{21.3.33}$$

whereas Launder, Reece, and Rodi [1975] (known as LRR method) proposed that the rapid pressure-strain for homogeneous turbulence may be correlated by

$$F_{ijkm} \overline{\nabla}_{k,m} = \alpha \left(A_{ij} - \frac{1}{3} A_{kk} \delta_{ij} \right) - \beta \left(G_{ij} - \frac{1}{3} G_{kk} \delta_{ij} \right) - \gamma \rho K d_{ij} \tag{21.3.34}$$

with

$$D_{ij} = \tau_{im}^* \overline{\nabla}_{m,j} + \tau_{jm}^* \overline{\nabla}_{m,i} \tag{21.3.35}$$

$$\alpha = \frac{8 + c_2}{11}, \qquad \beta = \frac{8c_2 - 2}{11}, \qquad \gamma = \frac{60c_2 - 4}{55}, \qquad 0.4 \le c_2 \le 0.6 \tag{21.3.36}$$

There are many other schemes for second order closure models. Among them are the tensor invariant method [Lumley, 1978], multi-scale method [Wilcox, 1988], nonlinear stress method [Speziale, Sarker, and Gatski, 1991], and modified LRR method [Launder, 1992].

21.3.5 ALGEBRAIC REYNOLDS STRESS MODELS

The purpose of algebraic Reynolds stress models is to avoid the solution of differential equations such as (21.3.23), and to obtain the Reynolds stress components directly from algebraic relationships. If mean strain rates are ignored in the Reynolds stress transport equations (21.3.23), it follows from the strain-dependent generalization of nonlinear constitutive relation that the turbulent stress tensor may be written as [Rodi, 1976; Gatski and Speziale, 1992],

$$\tau_{ij}^* = \frac{K}{\varepsilon} (D_{ij} + B_{ij}) \tag{21.3.37}$$

with

$$D_{ij} = c_1 \frac{\varepsilon}{K} \left(\tau_{ij}^* + \frac{2}{3} \rho K \delta_{ij} \right) \tag{21.3.38}$$

$$B_{ij} = -\frac{2}{3} \rho \varepsilon \delta_{ij} \tag{21.3.39}$$

Thus, if the mean strain rate vanishes, then we have

$$\tau_{ij}^* = -\frac{2}{3} \rho K \delta_{ij} \tag{21.3.40}$$

This suggests that the algebraic stress model is confined to isotropic turbulence. Thus, the algebraic stress model fails to properly account for sudden changes in the mean strain rate. If this algebraic Reynolds stress model is combined with the K–ε model,

however, it may be possible to obtain satisfactory results for secondary motions as reported by So and Mellor [1978] and Dumuren [1991].

A fully explicit, self-consistent algebraic expression for the Reynolds stress, which is the exact solution to the Reynolds stress transport equation in the weak equilibrium limit can be derived as shown by Girimaji [1995]. Preliminary tests indicate that the model performs adequately, even for three-dimensional mean flow cases.

21.3.6 COMPRESSIBILITY EFFECTS

The turbulent models discussed above are applicable to incompressible flows with time averages. For compressible flows, however, it is more convenient to use Favre averages than time averages as mentioned in Section 21.2. The Favre-averaged unknowns in (21.2.10) are modeled as follows:

Favre-averaged turbulent stress tensor

$$\tau_{ij}^* = -\overline{\rho v_i'' v_j''} = 2\mu_T \left(d_{ij} - \frac{1}{3} d_{kk} \delta_{ij} \right) - \frac{2}{3} \overline{\rho} K \delta_{ij} \tag{21.3.41}$$

Favre-averaged turbulent heat flux vector

$$q_i^* = \overline{\rho v_i'' H''} = -\frac{\mu_T c_p}{\mathrm{Pr}_T} \tilde{T}_{,i} = -\frac{\mu_T}{\mathrm{Pr}_T} \tilde{H}_{,i} \tag{21.3.42}$$

Favre-averaged turbulent molecular diffusion and turbulent transport

$$\overline{\tau_{ij} v_j''} - \frac{1}{2} \overline{\rho v_i'' v_j'' v_j''} = \left(\mu + \frac{\mu_T}{\sigma_k} \right) K_{,i} \tag{21.3.43}$$

The kinetic energy transport equations and Reynolds stress transport equations for compressible turbulent flows are written as follows:

Compressible turbulent kinetic energy transport equation

$$\frac{\partial \overline{\rho} K}{\partial t} + (\overline{\rho} \tilde{v}_i K)_{,i} = A_{(k)} + B_{(k)} + C_{(k)} + D_{(k)} \tag{21.3.44}$$

with

$$A_{(k)} = \tau_{ij}^* \tilde{v}_{j,i}$$

$$B_{(k)} = -\overline{\rho} \varepsilon$$

$$C_{(k)} = \left(\overline{\tau_{ij} v_j''} - \frac{1}{2} \overline{\rho v_i'' v_j'' v_j''} - \overline{p' v_i''} \right)_{,i}$$

$$D_{(k)} = -\overline{v_i''} \overline{p}_{,i} + \overline{p' v_{i,i}''}$$

The first three terms on the right-hand side of (21.3.44) are similar to the case of incompressible flows with extra terms in $D_{(k)}$ representing the pressure work and pressure dilatation due to density and pressure fluctuations.

Compressible Reynolds stress transport equation

$$\frac{\partial \tau_{ij}^*}{\partial t} + (\tilde{v}_k \tau_{ij}^*)_{,k} = A_{ij} + B_{ij} + C_{ij} + D_{ij} + \hat{D}_{ij} \tag{21.3.45}$$

with

$$A_{ij} = -\tau_{ij}^* \tilde{v}_{j,k} - \tau_{jk}^* \tilde{v}_{i,k}$$

$$B_{ij} = \overline{-\tau_{jk}^* v_{i,k}'' - \tau_{ik}^* v_{j,k}''}$$

$$C_{ij} = \left[\overline{\rho v_i'' v_j'' v_k''} + \overline{p' v_i''} \delta_{jk} + \overline{p' v_j''} \delta_{ik} - \overline{(\tau_{jk} v_i'' + \tau_{ik} v_j'')} \right]_{,k}$$

$$D_{ij} = -\overline{p'(v_{i,j}'' + v_{j,i}'')}$$

$$\hat{D}_{ij} = \overline{v_i''} \, \overline{p}_{,j} + \overline{v_j''} \, \overline{p}_{,i}$$

Here again the first four terms on the right-hand side of (21.3.45) have analogs for the incompressible flow with the last terms in $\hat{D}_{ij}$ for nonvanishing pressure gradients.

With additional new unknowns appearing in (21.3.44) and (21.3.45), we are faced with the difficult task of modeling them. Modeling in compressible turbulent flows for Reynolds averaged Navier-Stokes (RANS) system of equations has not been developed to a satisfactory extent. This is because the large-scale motions are difficult to model particularly in compressible flows. One way to resolve this problem is to use the large eddy simulation (LES) in which only subgrid (small) scales need be modeled. This will be discussed in Section 21.4.3.

Modifications From Incompressible Flows

Although the K–ε model has been applied to an incompressible flow with reasonable success, its performance in high-speed compressible flows met with difficulties. Sarkar et al. [1989] and Zeman [1990] independently proposed schemes which take into account the compressibility corrections by providing the so-called dilatational component ε_d in addition to the solenoidal component ε of the turbulence kinetic energy dissipation rate for the source term of the turbulence kinetic energy transport equation. Thus, (21.3.13a) is modified as

$$\frac{\partial}{\partial t}(\overline{\rho} K) + (\overline{\rho} K \overline{v}_i)_{,i} = (\mu_k K_{,i})_{,i} + (\overline{\tau}_{ij} \overline{v}_j)_{,i} - \overline{\rho}(\varepsilon + \varepsilon_d) \tag{21.3.46}$$

where

$$\varepsilon_d = \xi^* F(M_t) t$$

Sarkar Model
$$\xi^* = 1$$
$$F(M_t) = M_t^2$$
$$M_t = \frac{2K}{a^2} \quad \text{(Turbulent Mach Number)} \tag{21.3.47}$$

Zeman Model

$$\xi^* = \frac{3}{4}$$

$$F(M_t) = 1 - \exp\left[-\tfrac{1}{2}(\gamma + 1)(M_t - M_{to})^2/\lambda^2\right] H(M_t - M_{to})$$

$H =$ Heavy side step function

$$\left.\begin{array}{l} M_{to} = 0.1\,\sqrt{2/(\gamma + 1)} \\ \quad \lambda = 0.6 \end{array}\right\} \quad \text{free shear flows}$$

$$\left.\begin{array}{l} M_{to} = 0.25\,\sqrt{2/(\gamma + 1)} \\ \quad \lambda = 0.66 \end{array}\right\} \quad \text{wall boundary layers}$$

Wilcox [1992] suggests that the Sarkar model can be improved by using

$$\xi^* = \frac{3}{2}$$

$$F(M_t) = \left(M_t^2 - M_{to}^2\right) H\left(M_t - M_{to}\right)$$

$$M_{to} = \frac{1}{4}$$

The K–ω model with compressibility effects may be given by [Wilcox, 1992]

$$\frac{\partial}{\partial t}(\overline{\rho}K) + (\overline{\rho}K\overline{v}_i)_{,i} = [(\mu + \sigma^*\mu_T)K_{,i}]_{,i} + (\overline{\tau}_{ij}\overline{v}_i)_{,i} - \beta^*\rho\omega K \tag{21.3.48}$$

$$\frac{\partial}{\partial t}(\overline{\rho}\omega) + (\overline{\rho}\omega\overline{v}_i)_{,i} = [(\mu + \sigma^*\mu_T)\,\omega_{,i}]_{,i} + \alpha\frac{\omega}{K}(\overline{\tau}_{ij}\overline{v}_j)_{,i} - \beta\rho\omega\left[\omega + \hat{\xi}\,\sqrt{|2\Omega_{mn}\Omega_{mn}|}\right] \tag{21.3.49}$$

with

$$\omega = \frac{\varepsilon}{\beta^*K}, \qquad \beta^* = \beta_o^*\left[1 + \xi^*F(M_t)\right]$$

$$\mu_T = \frac{\rho K}{\omega}, \qquad \Omega_{mn} = \frac{1}{2}\left(\overline{v}_{i,j} - \overline{v}_{j,i}\right)$$

$$\beta = \beta_o - \beta_o^*\xi^*F(M_t)$$

where β_o^* and β_o are the corresponding incompressible values of β^* and β as given in (21.3.16).

Hanine and Kourta [1991] reported comparisons of the performance of various turbulence models to predict the near wall compressible flows and emphasized the importance of compressibility corrections. Wilcox [1992a] also studied the supersonic turbulent boundary layer flows. He showed that neither the Sarkar nor the Zeman compressibility term is completely satisfactory for both the compressible mixing layer and wall-bounded flows [Wilcox, 1992b]. The compressibility corrections cause a decrease in the effective von Karman constant, which yields the unwanted decrease in skin friction. However, for the K–ε model, the constant in the law of the wall varies with

density ratio in a nontrivial manner. Wilcox [1992] then combines Sarkar's simple functional dependence of dilatational dissipation on turbulence Mach number with Zeman's lag effect to produce a compressibility term that yields reasonably accurate predictions. Subsequently, Huang, Bradshaw, and Coarley [1992] reexamined the independent studies of Wilcox, Zeman, and Sarkar and concluded that the extension of incompressible turbulence models to compressible flow requires density corrections to the closure coefficients to satisfy the law of the wall. They further suggest that the K–ε model is more attractive than the K–ε model at high Mach numbers, because the coefficients of the unwanted density gradient terms are smaller. In view of these observations, the compressibility corrections which were originally developed for incompressible flows should be used with caution for applications into high-speed compressible turbulent flows.

The various turbulence models discussed in Section 21.3 represent a brief summary of historical developments for the period of nearly half a century. In Section 21.7, we present some limited numerical applications for the K–ε models. It appears, however, that the current interest in turbulence research is directed toward large eddy simulation and direct numerical simulation. We discuss these subjects in the following sections.

21.4 LARGE EDDY SIMULATION

Despite a great deal of effort and advancement in turbulence modeling for the past century, difficulties still remain in geometrically and physically complicated flowfields. The large eddy simulation (LES) is an alternative approach toward achieving our goal for more efficient turbulent flow calculations. Here, by using more refined meshes than usually required for Reynolds averaged Navier-Stokes (RANS) system of equations discussed in Section 21.3, large eddies are calculated (resolved) whereas small eddies are modeled. The rigor of LES in terms of performance and ability is somewhere between RANS of Section 21.3 and the direct numerical simulation (DNS) to be discussed in Section 22.5. There are two major steps involved in the LES analysis: filtering and subgrid scale modeling. Traditionally, filtering is carried out using the box function, Gaussian function, or Fourier cutoff function. Subgrid modeling includes eddy viscosity model, structure function model, dynamic model, scale similarity model, and mixed model, among others. These and other topics are presented below.

21.4.1 FILTERING, SUBGRID SCALE STRESSES, AND ENERGY SPECTRA

In order to define a velocity field containing only the large-scale components of the total field, it is necessary to filter the variables of the Navier-Stokes system of equations, resulting in the local average of the total field. To this end, using one-dimensional notation for simplicity, the filtered variable f may be written as

$$\overline{f} = \int G(x, \xi) f(\xi) d\xi \tag{21.4.1}$$

$$\text{with} \quad \int G(x, \xi) d\xi = 1$$

where $G(x, \xi)$ is the filter function which is large only when x and ξ are close together. They include box (tophat) function, Gaussian function, and Fourier cutoff function.

Box

$$G(x) = \begin{cases} 1/\Delta & \text{if } |x| \le \Delta/2 \\ 0 & \text{otherwise} \end{cases} \tag{21.4.2}$$

Gaussian

$$G(x) = \sqrt{\frac{6}{\pi \Delta^2}} \exp\left(-\frac{6x^2}{\Delta^2}\right) \tag{21.4.3}$$

Fourier cutoff

$$\hat{G}(k) = \begin{cases} 1 & \text{if } k \le \pi/2 \\ 0 & \text{otherwise} \end{cases} \tag{21.4.4}$$

The filtered momentum equation takes the form

$$\frac{\partial \overline{v}_j}{\partial t} + (\overline{v_i v_j})_{,i} = -\frac{1}{\rho}\overline{p}_{,j} + \overline{\tau}_{ij,i} \tag{21.4.5}$$

with

$$\begin{aligned}
\overline{v_i v_j} &= \overline{(\overline{v}_i + v'_i)(\overline{v}_j + v'_j)} = \overline{\overline{v}_i \overline{v}_j} + \overline{v'_i \overline{v}_j} + \overline{\overline{v}_i v'_j} + \overline{v'_i v'_j} \\
&= \overline{\overline{v}_i \overline{v}_j} + \overline{v}_i \overline{v}_j - \overline{v}_i \overline{v}_j + \overline{v'_i \overline{v}_j} + \overline{\overline{v}_i v'_j} + \overline{v'_i v'_j} \\
&= \overline{v}_i \overline{v}_j - \tau^*_{ij}
\end{aligned} \tag{21.4.6}$$

Substituting (21.4.6) into (21.4.5) yields

$$\frac{\partial \overline{v}_j}{\partial t} + (\overline{v}_i \overline{v}_j)_{,i} = -\frac{1}{\rho}\overline{p}_{,j} + \overline{\tau}_{ij,i} + \tau^*_{ij,i}$$

with the subgrid stress tensor τ^*_{ij} identified from (22.4.6) as

$$-\tau^*_{ij} = L_{ij} + C_{ij} + R_{ij} = \overline{v_i v_j} - \overline{v}_i \overline{v}_j \tag{21.4.7}$$

where L_{ij}, C_{ij}, and R_{ij} are known as the Leonard stress tensor, cross stress tensor, and subgrid scale Reynolds stress tensor, respectively.

$$\begin{aligned}
L_{ij} &= \overline{\overline{v}_i \overline{v}_j} - \overline{v}_i \overline{v}_j \\
C_{ij} &= \overline{v'_i \overline{v}_j} + \overline{\overline{v}_i v'_j} \\
R_{ij} &= \overline{v'_i v'_j}
\end{aligned} \tag{21.4.8}$$

Here, the Leonard stress represents the interaction between resolved scales, transferring energy to small scales (known as outscatter). The Leonard stress can be computed explicitly from the filtered velocity field. The cross stress represents the interaction between resolved and unresolved scales, transferring energy to either large or small scales. The subgrid scale Reynolds stress represents the interaction of two small scales, producing energy from small scales to large scales (known as backscatter).

The cross stress tensor may be simplified in terms of resolved scales using the so-called Galilean scale similarity model [Bardina et al., 1980],

$$C_{ij} = \overline{v_i' \overline{v}_j} + \overline{\overline{v}_i v_j'} = \overline{\overline{v}_i \overline{v}_j} - \overline{v}_i \overline{v}_j \tag{21.4.9a}$$

Summing (22.4.8a) and (22.4.9a) leads to

$$K_{ij} = L_{ij} + C_{ij} = \overline{\overline{v}_i \overline{v}_j} - \overline{\overline{v}}_i \overline{\overline{v}}_i \tag{21.4.9b}$$

It is seen that the sum of the Leonard and cross stresses can be calculated from the resolved scales and thus only the subgrid scale Reynolds stress need be modeled. Thus, the turbulent stress tensor to be modeled is given by (21.4.6) or (21.4.7) as

$$\tau_{ij}^* = -(\overline{v_i v_j} - \overline{v}_i \overline{v}_j) \tag{21.4.10}$$

Before we discuss subgrid scale models, it is informative to examine the physical significance of the filtering in terms of the Kolmogorov' "−5/3 law" for the energy spectrum [Kolmogorov, 1941]. The energy spectrum $E(\kappa)$ is related by the turbulent kinetic energy,

$$K = \frac{1}{2}\overline{v_i' v_i'} = \int_0^\infty E(\kappa) d\kappa \tag{21.4.11}$$

The distribution of energy spectrum $E(\kappa)$ vs wave number κ is divided into three regions as shown in Figure 21.4.1: the region of energy containing large eddies, followed by the inertial subrange and energy dissipation range, between the wave numbers identified by the reciprocals of the energy bearing length scale ℓ (integral scale) and the Kolmogorov microscale η,

$$\eta = (\nu^3 / \varepsilon)^{1/4} \tag{21.4.12}$$

Note that the inertial subrange is characterized by a straight line, known as the Kolmogorov's "−5/3 law,"

$$E(\kappa) = \alpha \varepsilon^{2/3} \kappa^{-5/3} \tag{21.4.13}$$

where α is a constant. In this range, eddies are small and dissipation becomes important at smallest scales. Thus, the filtering process is designed to identify this range with a
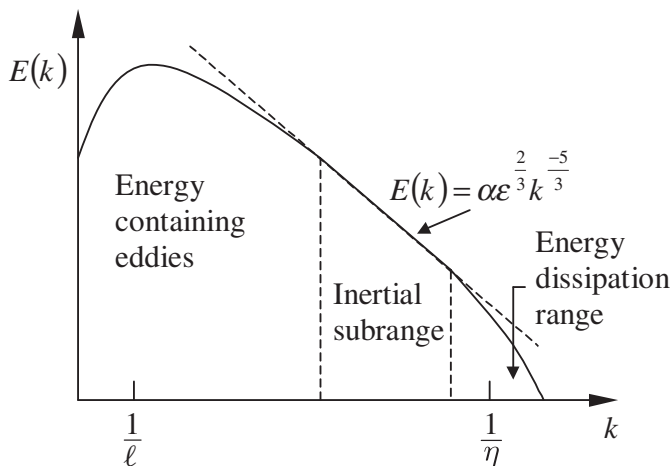

Figure 21.4.1   Energy spectrum vs. wave number space (log-log scales).

suitable filter width. In what follows, our discussion will be based on filtering by the box function.

21.4.2 THE LES GOVERNING EQUATIONS FOR COMPRESSIBLE FLOWS

The Navier-Stokes system of equations for LES may be written in terms of Favre averages using the filtering process presented in Section 22.4.1. The filtered continuity, momentum, and energy equations for compressible flows are described below.

Construction of turbulent closure models for high Mach numbers and high Reynolds numbers in hypersonic flows is difficult, particularly for large turbulence scales. For this reason, one may wish to explore the possibility of LES in the hope that the subgrid scale (SGS) modeling is still feasible. To this end, we rewrite the Favre-filtered compressible flow governing equations as follows:

$$\frac{\partial \overline{\rho}}{\partial t} + (\overline{\rho}\tilde{v}_i)_{,i} = 0 \tag{21.4.14a}$$

$$\frac{\partial}{\partial t}(\overline{\rho}\tilde{v}_j) + (\overline{\rho}\tilde{v}_i\tilde{v}_j)_{,i} + \overline{p}_{,j} - (\overline{\tau}_{ij} + \tau_{ij}^*)_{,i} = \mathbf{0} \tag{21.4.14b}$$

$$\frac{\partial}{\partial t}(\overline{\rho}\tilde{E}) + [(\overline{\rho}\tilde{E} + \overline{p})\tilde{v}_i - \tilde{\tau}_{ij}\tilde{v}_j + \tilde{q}_i]_{,i} + (q_i^{(H)} + q_i^{(T)} + q_i^{(v)})_{,i} = 0 \tag{21.4.14c}$$

where the SGS variables are the turbulent stress τ_{ij}^*, turbulent heat flux $q_i^{(H)}$, turbulent diffusion $q_i^{(T)}$, and turbulent viscous diffusion $q_i^{(V)}$. They are expressed as

$$\boldsymbol{\tau}_{ij}^* = -\overline{\rho}\left(\widetilde{v_i v_j} - \tilde{v}_i\tilde{v}_j\right)$$

$$q_i^{(H)} = \overline{\rho}\tilde{c}_p(\widetilde{v_i T} - \tilde{v}_i\tilde{T})$$

$$q_i^{(T)} = \frac{1}{2}\overline{\rho}\left(\widetilde{v_i v_j v_j} - \tilde{v}_i\tilde{v}_j\tilde{v}_j\right) \tag{21.4.15a,b,c,d}$$

$$q_i^{(v)} = -(\overline{\tau_{ij}v_j} - \tilde{\tau}_{ij}\tilde{v}_j)$$

These unknown variables may be modeled by several different ways. Among them are (1) eddy viscosity model, (2) scale similarity model, and (3) mixed model. We describe these methods in the next section.

21.4.3 SUBGRID SCALE MODELING

The solution of the filtered Navier-Stokes system of equations enables only the large eddies to be resolved, leaving the small eddies still unresolved. Since these small eddies are more or less isotropic, the modeling is much easier than in the case of RANS. However, for compressible flows, particularly for supersonic and hypersonic flows in which turbulent heat flux, turbulent diffusion, and viscous diffusion may become significant, the SGS modeling process is far from satisfactory.

There are three different approaches for developing the SGS turbulent stress models. The eddy viscosity model is most widely used in which the global effect of SGS terms is taken into account, neglecting the local energy events associated with convection and diffusion [Smagorinsky, 1963; Yoshizawa, 1986; Moin et al., 1991; Gao and O'Brien, 1993].

The scale similarity model assumed that the most active subgrid scales are those close to the cutoff wave number and uses the smallest resolved SGS stresses. This approach does account for the local energy events, but tends to underestimate the dissipation [Bardina et al., 1980].

To compensate the drawbacks of the eddy viscosity model and scale similarity model, Erlebacher et al. [1992] proposed the mixed model in which the dissipation is adequately provided to the scale similarity model.

Germano [1992] proposed that the closure constants involved in the SGS turbulent stress tensors be calculated dynamically (flowfield dependent), known as the dynamic model. The advantage of the dynamic model has been demonstrated by many investigators.

Attempts have been made to provide SGS modeling for turbulent diffusion and viscous diffusion in the energy equation by some investigators. Among them are Normand and Lesieur [1992], Meneveau and Lund [1997], and Knight et al. [1998].

In what follows, we introduce some of the well-known models of SGS turbulent eddy viscosity, turbulent heat flux, and turbulent diffusion.

SGS Eddy Viscosity Model for Stress Tensor with Time Averages

In this model, the traditional gradient-diffusion approach (molecular motion) is used so that the turbulent stress tensor for compressible flows is written as

$$\tau_{ij}^* = 2\mu_T\left(\overline{d}_{ij} - \frac{1}{3}\overline{d}_{kk}\delta_{ij}\right) - \frac{2}{3}\overline{K}\delta_{ij} \tag{21.4.16}$$

$$\mu_T = \overline{\rho}(C_s\Delta)^2|\overline{d}|, \qquad \Delta \cong \ell, \qquad \overline{d}_{ij} = \frac{1}{2}(\overline{v}_{i,j} + \overline{v}_{j,i}), \qquad |\overline{d}| = (2\overline{d}_{ij}\overline{d}_{ij})^{1/2}$$

where C_s is the Smagorinsky constant and $\overline{K}$ is the subgrid scale turbulent kinetic energy. This constant can be evaluated by assuming the existence of an inertial range spectrum given in Figure 21.4.1. To this end, it has been suggested in [Lilly, 1966] that

$$|\overline{d}|^2 \cong 2\int_0^{\pi/\Delta} \kappa^2 E(\kappa)d\kappa = 2C_k\varepsilon^{2/3}\int_0^{\pi/\Delta} \kappa^{1/3}d\kappa = \frac{3}{2}C_k\varepsilon^{2/3}\left(\frac{\pi}{\Delta}\right)^{4/3} \tag{21.4.17}$$

where $C_k = 1.41$ is the Kolmogorov constant. Thus, we arrive at

$$C_s \cong \frac{1}{\pi}\left(\frac{2}{3\alpha}\right)^{3/4} = 0.18 \tag{21.4.18}$$

The isotropic parts, $\overline{K}$ and $\overline{d}_{kk}$ terms, on the right-hand side of (22.4.16) may be neglected for incompressible flows. For further details on the subgrid scale modeling for the isotropic parts in compressible flows, see Squires [1991], Erlebacher et al. [1992], and Vreman, Geurts, and Kuerten [1995].

SGS Eddy Viscosity Model for Stress Tensor with Favre Averages

The subgrid scale stress tensor as given by (21.4.15a) may now be written for the compressible flow Favre averages as

$$\tau_{ij}^* = -\overline{\rho}(\overline{\overline{v_i v_i}} - \tilde{v}_i\tilde{v}_i) = 2\mu_T\left(\tilde{d}_{ij} - \frac{1}{3}\tilde{d}_{kk}\delta_{ij}\right) - \frac{2}{3}\tilde{K}\delta_{ij} \tag{21.4.19}$$

with

$$\mu_T = \overline{\rho}(C_s\Delta)^2|\tilde{d}|$$
$$\tilde{K} = \overline{\rho}C_I\Delta^2|\overline{d}|^2$$

(21.4.20)

with $C_s = 0.16$ and $C_I = 0.09$.

Moin et al. [1991] extended the Germano's dynamic model [Germano, 1992] for Favre averages. The Favre averaged mixed model was developed by Speziale, Zang, and Hussaini [1988] and used by Erlebacher et al. [1992].

SGS Structure Function Model

Metais and Lesieur [1992] proposed the structure function model in the form

$$\nu_T = 0.105 C_k^{-3/2}\Delta x[F(\mathbf{x}, \Delta x)]^{1/2}$$

(21.4.21)

where F is calculated as

$$F(\mathbf{x}, \Delta\Omega) = \frac{1}{6}\sum_{i=1}^{3}\left[\|u(\mathbf{x}) - u(\mathbf{x}+\Delta x_\mathbf{i}\mathbf{i_i})\|^2 + \|u(\mathbf{x}) - u(\mathbf{x}-\Delta x_\mathbf{i}\mathbf{i_i})\|^2\right]\left(\frac{\Delta\Omega}{\Delta\Omega_i}\right)^{2/3}$$

(21.4.22)

with $\Delta\Omega = (\Delta x_1\Delta x_2\Delta x_3)^{1/3}$. In the limit of $\Delta x \to 0$, Comte [1994] suggested that

$$\nu_T \cong 0.777(C_s\Delta x)^2\sqrt{2\overline{d}_{ij}\overline{d}_{ij} + \overline{\omega}_i\overline{\omega}_i}$$

(21.4.23)

where C_s is the Smagoronsky's constant and $\overline{\omega}_i$ is the vorticity of the filtered field.

Dynamic SGS Eddy Viscosity Model with Time Averages

It has been shown in the literature that superior results may be obtained by updating the model coefficients based on the current flowfields, known as the dynamic model [Germano, Piomelli, Moin, and Cabot, 1991]. Here, in addition to the subgrid scale filtering, a test filter is introduced with the test filter width Δ_t larger than the grid filter width Δ (usually $\Delta_t = 2\Delta$ is used) in order to obtain information from the resolved flowfield. Based on this model, Lilly [1992] suggested that

$$\mu_T = C_d\overline{\rho}\Delta^2|\overline{d}|$$

(21.4.24)

with

$$C_d = \frac{A_{ij}M_{ij}}{M_{km}M_{km}}$$

(21.4.25)

$$A_{ij} = \langle\overline{\rho v_i v_j}\rangle - \frac{\langle\overline{\rho v_i}\rangle\langle\overline{\rho v_j}\rangle}{\langle\overline{\rho}\rangle}$$

$$M_{ij} = -2\Delta_t^2\langle\overline{\rho}\rangle\langle|\overline{d}|\rangle\left\langle\overline{d}_{ij} - \frac{1}{3}\overline{d}_{kk}\delta_{ij}\right\rangle + 2\Delta^2\left\langle\overline{\rho}|\overline{d}|\left(\overline{d}_{ij} - \frac{1}{3}\overline{d}_{kk}\delta_{ij}\right)\right\rangle$$

where $\langle\ \rangle$ implies a test filtered quantity.

The test filter operation can be performed as

$$\langle f(x, t)\rangle = \int \langle G(x, \xi)\rangle f(\xi, t)d\xi \tag{21.4.26}$$

If the box function is used, we have

$$\langle G(x - \xi)\rangle = \begin{cases} \dfrac{1}{\Delta_t} & \text{if } x_i - \Delta_t/2 \leq \xi_i \leq x_i + \Delta_t/2 \\ 0 & \text{otherwise} \end{cases} \tag{21.4.27}$$

The test filter can be calculated using the trapezoidal rule, Simpson's rule, or interpolation function methods. For example, the one-dimensional filtering operation with the trapezoidal rule assumes the form,

$$\langle f_i\rangle = \frac{1}{\Delta_t}\int_{x-\Delta_t/2}^{x+\Delta_t/2} f(\xi)d\xi = \frac{1}{4}(f_{i-1} + 2f_i + f_{i+1}) \tag{21.4.28}$$

We then apply this one-dimensional approximation successively in each coordinate direction for multidimensional problems.

SGS Heat Flux Closure with Favre Averages

The subgrid scale modeling for the energy equation has not received much attention. This is because, for low Mach number flows, the effect of turbulence modeling is negligible. For high Mach number flows, we may use the standard gradient diffusion model (eddy viscosity)

$$q_i^{(H)} = \overline{\rho}\tilde{c}_p(v_i T - \tilde{v}_i \tilde{T}) = \frac{\overline{\rho}\tilde{c}_{pT}}{\mathrm{Pr}_T}\tilde{T}_{,i} \tag{21.4.29}$$

with

$$v_T = C\Delta^2|\tilde{d}| \tag{21.4.30}$$

The eddy viscosity in (21.4.30) may be expressed dynamically as shown in (21.4.25).

SGS Turbulent Diffusion and Viscous Diffusion Closures

Vreman et al. [1995] shows further details of subgrid modeling for the energy equation using the Fabre averaged variables. The SGS turbulent diffusion closure has been proposed by Knight et al. [1998] and the SGS viscous diffusion closure model studied by Meneveau and Lund [1997]. The scale similarity approach was applied in both cases. Future developments in these areas are needed to substantiate the accuracy of models, particularly for high Reynolds number and high Mach number hypersonic flows.

As a result of the LES solution of the Navier-Stokes system of equations, we obtain the flow variables which contain not only the mean quantities but also the fluctuations. We then compute the mean flowfield values by various schemes of averaging or filtering methods (time averages, spatial averages, or filtered Favre averages, etc.). The difference between the LES solution and the averages will lead to the turbulence fluctuations. From these fluctuations, detailed turbulence statistics can be computed. Among them are the turbulent intensities, distributions of energy spectra with respect to wave numbers, production, dissipation, and diffusion of turbulent kinetic energy and Reynolds stresses,

compressibility effects as reflected by dilatation, high-speed flow heat transfer, details of shock wave turbulent boundary layer interactions through transition to full turbulence, and physics of relaminarization. Some examples on LES computations will be presented in Section 22.8, Applications.

21.5 DIRECT NUMERICAL SIMULATION

21.5.1 GENERAL

As we have seen in the previous chapters, turbulence modeling is not an easy task. Even in large eddy simulation, in which we only need to model small scales of isotropic motions, the process becomes complicated in dealing with energy equation for high-speed compressible flows. Thus, our final resort may seem to be a direct numerical solution in which no turbulence modeling is needed. However, we require excessive mesh refinements and higher order accurate numerical schemes. The computational cost for DNS particularly in high-speed compressible flows will be prohibitive.

In direct numerical simulations (DNS), the Navier-Stokes system of equations is solved directly with refined meshes capable of resolving all turbulence length scales including the Kolmogorov microscale,

$$\eta = (\nu^3/\varepsilon)^{1/4} \tag{21.5.1}$$

All turbulence scales ranging from the large energy-containing eddies to the dissipation scales,

$$0.1 \leq k\eta \leq 1$$

with k being the wave number must be resolved (see Figure 21.4.1). To meet this requirement, the number of grid points required is proportional to $L/\eta \approx \mathrm{Re}^{3/4}$ where L is the characteristic length and Re is the Reynolds number referenced to the integral scale of the flow. This leads to the number of grid points in 3-D to be proportional to

$$N = \mathrm{Re}^{9/4} \tag{21.5.2}$$

The number of grid points required for a channel flow may be estimated in terms of turbulence Reynolds number Re_T [Moser and Moin, 1984; Kim, Moin, and Moser, 1987] as

$$N = (3\mathrm{Re}_T)^{9/4} \tag{21.5.3}$$

with

$$\mathrm{Re}_T = \frac{u_T H}{2\nu} \tag{21.5.4}$$

where u_T is the shear velocity (approximately 5% of the mean average velocity) and H is the channel height.

Similarly, the time step is limited [Kim et al., 1987] by the Kolmogorov time scale, $\tau = (\nu/\varepsilon)^{1/2}$, as

$$\Delta t \cong \frac{0.003 H}{u_T \sqrt{\mathrm{Re}_T}} \tag{21.5.5}$$

These restrictions are clearly too severe for DNS to be a practical design tool in industry in view of currently available computer capacity.

21.5.2   VARIOUS APPROACHES TO DNS

The DNS applications have been carried out most successfully using spectral methods in simple geometries. Fourier series are applied to the streamwise and spanwise directions whereas Chebyshev polynomials or B-splines are used for the wall-normal direction. However, the spectral methods are not suitable for practical industrial problems with complex geometries and boundary conditions. The use of FDM, FEM, or FVM, although not as accurate as spectral methods, is more flexible in handing arbitrary geometries and boundary conditions. In view of the fact that turbulence is three-dimensional in nature and DNS requires excessive grid refinements, FDM calculations with uniform structured grids have been used predominantly in the past. DNS in unstructured arbitrary practical geometries and boundary conditions at high Reynolds number flows are severely limited by available computer resources.

Applications of DNS in incompressible or subsonic flows and compressible or supersonic flows are distinguished by several factors: (1) For incompressible simulations, the viscous terms are treated usually implicitly, allowing the viscous stability limit to be relaxed, whereas for compressible flows the time discretization is explicit and the allowable time step is limited by the viscous stability limit rather than by the convection condition; (2) Toward transition to turbulence, instability growth rates are slower in compressible flows than in incompressible flows. This will require longer time integration; (3) High-speed transitional disturbance modes have high gradients for compressible flows requiring much more mesh refinements and higher order accuracy in spatial approximations than for incompressible flows.

In DNS, we may use either the temporal or spatial simulation approach. The temporally evolving simulation is usually limited to periodic inflow and outflow boundary conditions and a parallel flow without the consideration of the boundary layer growth. The spatially evolving approach is more general and practical in which nonperiodic inflow and outflow boundary conditions are used and the evolution of nonparallel boundary layer is accounted for. Some recent advancements for both temporally and spatially evolving simulations are reported in Guo, Kleiser, and Adams [1996].

The earlier works on transition and turbulence in boundary layer flows using DNS include Kim, Moin, and Moser [1985], Spalart and Yang [1987], Fasel, Rist, and Konzelmann [1990], Rai and Moin [1993], among others.

The DNS solution of the Navier-Stokes system of equations provides the flow variables which contain not only the mean quantities but also the fluctuations similarly as in LES discussed in Section 21.4. The objective of DNS is to obtain more accurate results for turbulence statistics than in LES at the expense of computing costs. Since the disadvantages resulting from possible inadequate subgrid scale modeling are eliminated in DNS, it is anticipated that the DNS results may be used as a guidance of improving any or all modeling processes for turbulence presented in the previous sections. Details of applications in DNS will be presented in Section 21.7.

21.6 SOLUTION METHODS AND INITIAL AND BOUNDARY CONDITIONS

Although explicit methods may be used in turbulent flows in general, it is often necessary to employ implicit methods in order to handle viscosity in wall-bounded turbulence. Various numerical schemes such as Runge-Kutta, Crank-Nicolson, Adams-Brashforth, among others, have been used in RANS, LES, and DNS calculations using FDM and FVM via FVM. For FEM formulations, the FEM equations may be solved using conjugate gradient or GMRES.

Initial and boundary conditions in turbulent flows are more sensitive to the solution as compared with laminar flows. This is because a small change in the initial state of turbulent flow is amplified exponentially in time. Since this is physical rather than numerical, it is difficult to assess the numerical error if one changes the numerical methods to improve the numerical methods or refine the mesh to obtain more accurate results. So, the question is: how do we know if we have a good solution? This question can be answered with reference to Figure 21.4.1. If the energy spectrum in the smallest scales with the wave number larger than the inertial subrange is much smaller than the peak in the smaller wave number region, then we may assume that the solution is satisfactory.

For inflow initial and boundary conditions, periodic boundary conditions are convenient to use (particularly suitable for spectral methods) if flows do not vary in a given direction. Otherwise, the initial and boundary conditions may be obtained from other simulations, adopted from isotropic turbulence.

For outflow boundaries, one may use the extrapolation conditions, requiring the derivatives of all variables normal to the surface set equal to zero,

$$(\rho u)_{,i} n_i = 0 \qquad (21.6.1)$$

If the flow is unsteady, then it appears that time-dependent boundary conditions be implemented by enforcing the time-dependent mass flux conservation at the outflow boundary,

$$\Delta(\rho u) = -\Delta t u_0 (\rho u)_{,i} n_i \qquad (21.6.2)$$

with u_0 being the average velocity of the outflow boundary. This tends to keep the reflected pressure waves from moving back to the domain.

On the solid boundary, the standard no-slip condition can be applied. Because of turbulence microscales close to the wall leading to complicated turbulent structures including separated flows, one must use highly refined meshes adjacent to the wall. Furthermore, in this region, turbulence may remain unsteady even when the flow away from the wall has reached a steady state.

In DNS and LES, the resolved flow may become unsymmetric even if the geometry and the flow boundary conditions are symmetric. Thus, the symmetry condition should not be used in the simulation of turbulence using DNS or LES.

As we have seen in multigrid methods (Section 20.2) in which low frequency (small wave number) errors are eliminated in coarse mesh, large-scale turbulence can be resolved quickly in the coarse mesh so that computational efficiency can be realized if the

solution is then performed on the fine mesh subsequently. This suggests that multigrid methods are particularly useful in DNS and LES.

21.7 APPLICATIONS

21.7.1 TURBULENCE MODELS FOR REYNOLDS AVERAGED NAVIER-STOKES (RANS)

Exhaustive numerical demonstrations for turbulence model applications are not attempted in this section. Instead, we focus on some representative incompressible flow applications for RANS. In this illustration, we introduce the work of Thangam and Speziale [1992] which shows the comparison of various types of K–ε models as applied to the backward-facing step shown in Figure 21.7.1.1a. The finite volume method via FDM [Thangam and Hur, 1991] is employed with a computational grid of 200×100 mesh (a coarser version is shown in Figure 21.7.1.1b) and Re $= 1.32 \times 10^5$. Computed results for the standard K–ε model with the wall boundary conditions of the two-layer case are shown in Figure 21.7.1.2a.

   As compared with the experimental data of Kim, Kline, and Johnston [1980], it is seen that reattachment length for the two-layer model ($X_r = 6.0$) is about 15% underestimated (experimental value, $X_r = 7.1$, from Kim et al [1980]). Despite this discrepancy, the mean velocity profiles appear to be in good agreement (Figure 21.7.1.2b), although the turbulent intensity profiles (Figure 21.7.1.2c) and shear stress profiles (Figure 21.7.1.2d) show some deviations from the experimental data.

   For the three layer model, the reattachment length is $X_r = 6.25$ (Figure 21.7.1.3a), about 5% improvement from the two-layer case. Mean velocity profiles (Figure 21.7.1.3b), turbulent intensity profiles (Figure 21.7.1.3c), and shear stress profiles (Figure 21.7.1.3d) appear to be the same as in the two-layer model.

(a) Physical configuration and coordinate system

(b) Computational grid: Y/H=3, Re=1.32×10⁵, 200×100 mesh
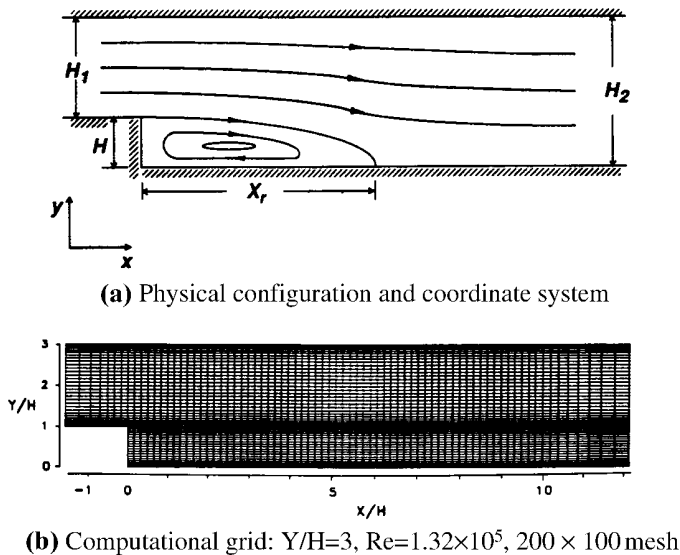
Figure 21.7.1.1 Incompressible turbulent flow backward facing step, 2-D geometry for K–ε model analysis, $C_\mu = 0.09$, $C_{\varepsilon 1} = 1.44$, $C_{\varepsilon 2} = 1.92$, $\sigma_k = 1.92$, $\sigma_\varepsilon = 1.0$, CD $= 1.68$ [Thangam and Speziale, 1988].
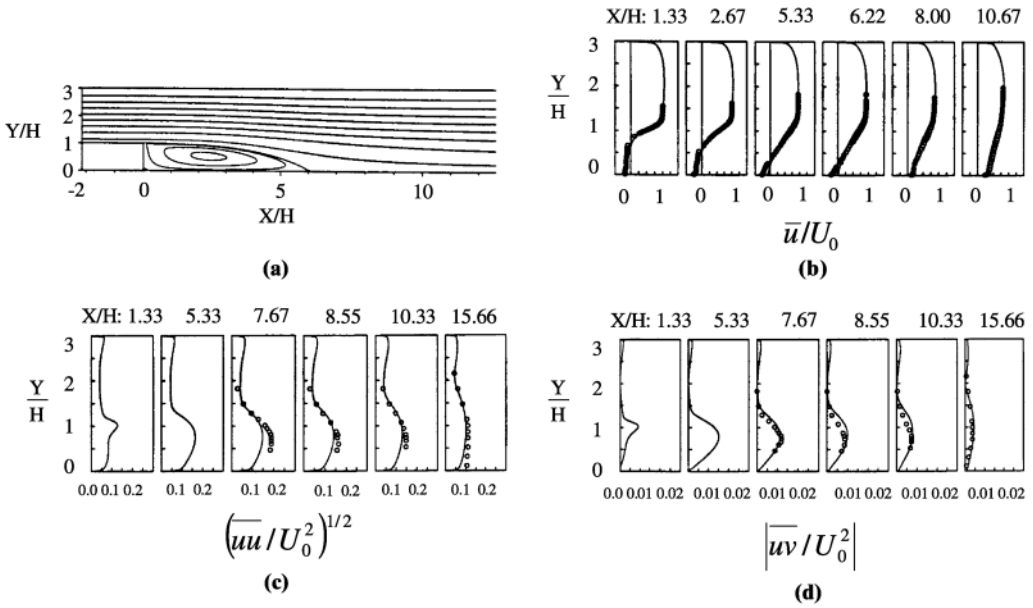
Figure 21.7.1.2 Results with the standard K–ε two-layer model [Thangam and Speziale 1988], compared with Kim et al. [1980]. **(a)** Contours of mean streamlines. **(b)** Mean velocity profiles at selected locations, compared with experiments [Kim et al., 1980]. **(c)** Turbulence intensity profiles. **(d)** Turbulence shear stress profiles.
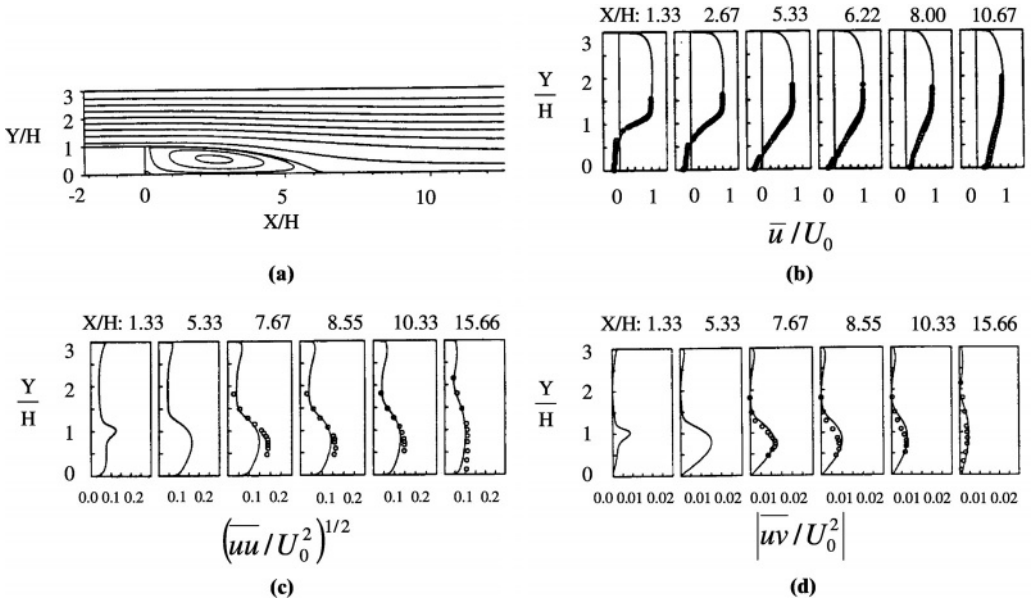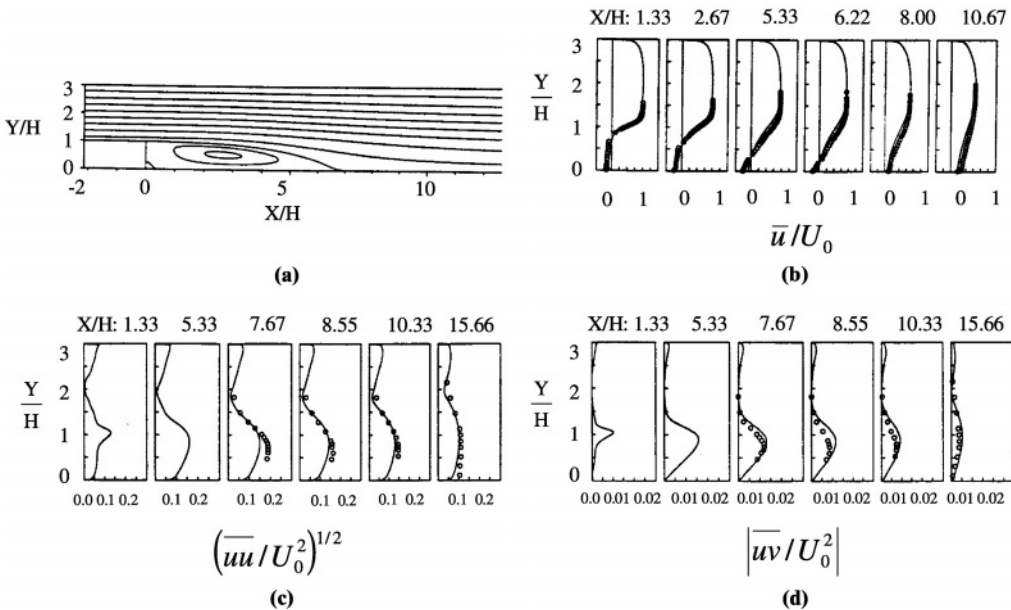

Figure 21.7.1.3 Results with the standard K–ε three-layer model [Thangam and Speziale, 1988]. **(a)** Contours of mean streamlines. **(b)** Mean velocity profiles at selected locations, compared with experiments [Kim et al., 1980]. **(c)** Turbulence intensity profiles. **(d)** Turbulence shear stress profiles.

Figure 21.7.1.4 Results with the nonlinear (anisotropic) K–ε three-layer model [Thangam and Speziale, 1988]. **(a)** Contours of mean streamlines. **(b)** Mean velocity profiles at selected locations, compared with experiments [Kim et al., 1980]. **(c)** Turbulence intensity profiles. **(d)** Turbulence shear stress profiles.

It is interesting to note that significant improvements for the reattachment length ($X_r = 6.9$), only 3% deviation from the experimental data, arise when the nonlinear (anisotropic) K–ε model is used (Figure 21.7.1.4a). Other data for the mean velocity, turbulent intensity, and shear stress profiles (Figure 21.7.1.4b,c,d) still show some deviations from the experiments.

21.7.2 LARGE EDDY SIMULATION (LES)

(1) Incompressible Flows

We consider here turbulent incompressible flows for a 3-D backward-facing step geometry (Figure 21.7.2.1) using LES as reported by Fureby [1999]. In this example, the results of the various LES models including the Smagorinsky model (SMG), dynamic
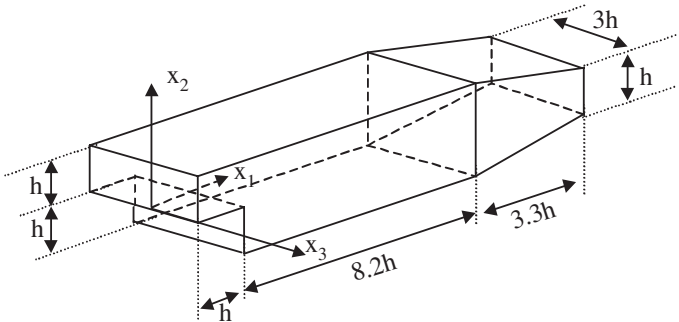
Figure 21.7.2.1 Backward-facing step 3-D geometry for LES analysis [Fureby, 1999].

Table 21.7.2.1 Overview of Simulations, Grids, and Global Quantities

Case/ run	Re, $\times 10^4$	SGS mode	Grid; resolution	λ/h	$\partial\delta_\omega/\partial x_1$	Sr, $x_1/$ $h=1$	Sr, $x_1/$ $h=6$	Ξ, $x_1/$ $h=3$
A1	1.5	OEEVM	87,104;2Δ	6.8	0.25	0.20	0.07	0.13
A2	1.5	OEEVM	204,460;3Δ/2	6.6	0.26	0.19	0.07	0.10
B1	2.2	OEEVM	366,750;3Δ/2	7.1	0.27	0.23	0.06	0.11
B2	2.2	OEEVM	170,400;2Δ	7.1	0.25	0.23	0.06	0.16
B3	2.2	SMG	170,400;2Δ	7.2	0.24	0.22	0.07	0.17
B4	2.2	DSMG	170,400;2Δ	7.1	0.27	0.24	0.07	0.17
B5	2.2	MILES	170,400;2Δ	7.4	0.25	0.23	0.05	0.15
B6	2.2	OEEVM	1,152,600; Δ	7.0	0.28	0.23	0.06	0.06
C1	3.7	OEEVM	366,750;2Δ	6.9	0.26	0.25	0.06	0.17
Exp*	1.5	—	—	6.5	0.28	—	—	—
Exp*	2.2	—	—	7.0	0.28	—	—	—
Exp*	3.7	—	—	6.8	0.28	—	—	—

*Pitz and Daily [1981].

Smagorinsky model (DSM), one-equation eddy viscosity model (OEEVM) [Lesieur and Metais, 1996], and monotonically integrated large eddy simulation (MILES) [Fureby, 1999] are compared with those of the experimental results of Pitz and Daily [1981]. In MILES, the Navier-Stokes system of equations are solved using the monotonic integration with flux limiters in which high-resolution monotone methods with embedded nonlinear filters providing implicit closure models so that explicit SGS models need not be used. Various test cases are summarized in Table 21.7.2.1.

Contours of streamwise instantaneous velocity as shown in Figure 21.7.2.2a indicate the free shear layer terminating at approximately $x_1/h \cong 7$. Figure 21.7.2.2b shows the
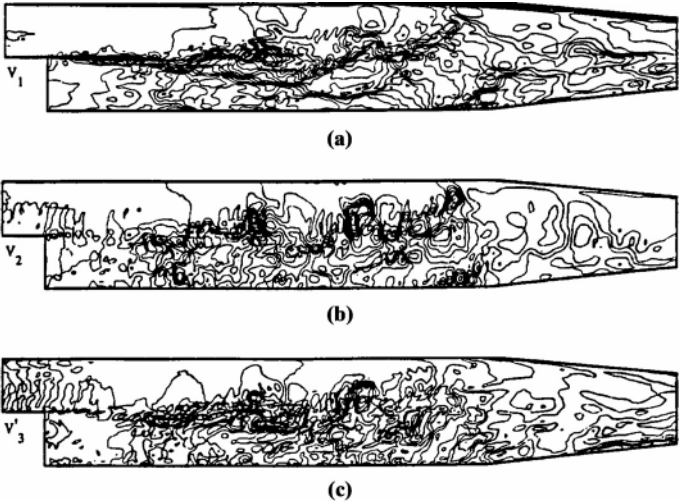

Figure 21.7.2.2 Instantaneous velocity and velocity fluctuation contours in the centerplane [Fureby, 1999]. **(a)** Streamwise velocity component. **(b)** Vertical velocity component. **(c)** Spanwise velocity component.
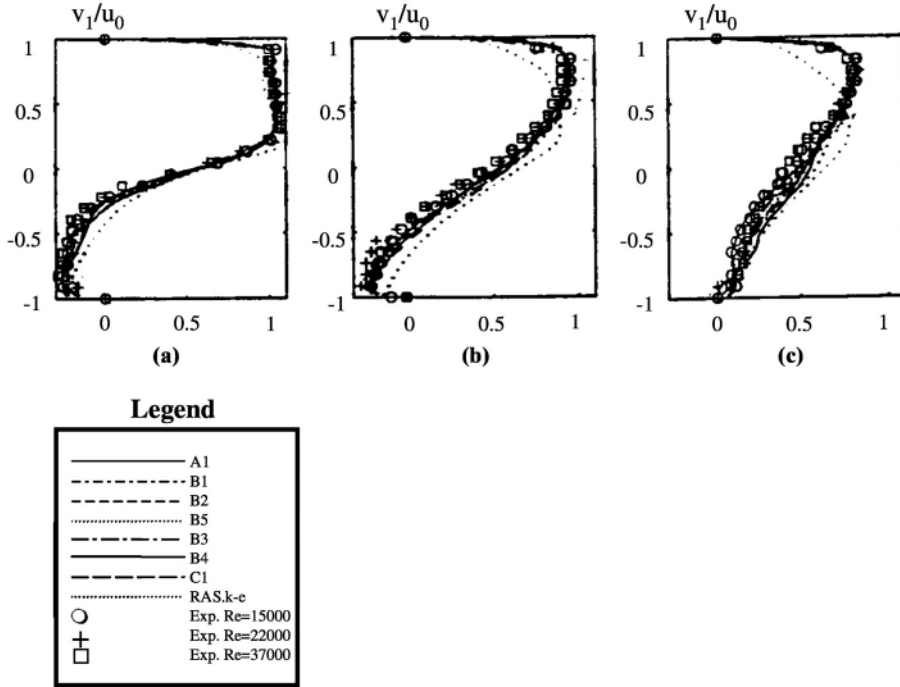
Figure 21.7.2.3   Streamwise mean velocity profiles $< \overline{v}_1 >$ downstream of the step at **(a)** $x_1/H = 2$, $Re = 15 \times 10^3$ **(b)** $x_1/H = 5$, $Re = 22 \times 10^3$, and **(c)** $x_1/H = 7$, $Re = 37 \times 10^3$ [Fureby, 1999].

vertical flow patches, with alternating positive and negative $\overline{v}_2$ regions of spanwise Kelvin-Helmoltz vortices. Spanwise velocity fluctuations are shown in Figure 21.7.2.2c, with peak values reaching as high as $0.5\, u_0$ near reattachment. The near wall region appears laminar-like in the simulation as well as in the experiment [Pitz and Daily, 1981].

Streamwise mean velocity profiles at various downstream locations are shown in Figure 21.7.2.3. The results of MILES and LES results using OEEVM, SMG, and DSMG models are compared with the experimental data [Pitz and Daily, 1981] for various cases given in Table 21.7.2.1. It is seen that all LES models perform well as compared with the experimental data, whereas the K–ε model deviates considerably toward townstream.

Figure 21.7.2.4 shows the power density spectra as a function of the nondimensional frequency or the Strouhal number $Sr = fh/\overline{v}_1$. Spectra are presented at two locations downstream of the step for run B1 (Figure 21.7.2.4a,b), for different Reynolds numbers (Figure 21.7.2.4c) and for different SGS models (Figure 21.7.2.4d). Note that all spectra exhibit a well-defined $Sr^{-5/3}$ range over one decade. The energy in the smaller scales is found to be more evenly distributed among the velocity components (Figure 21.7.2.4a,b), indicating a trend toward isotropy. The energy distribution in the larger scales is anisotropic, the $\overline{v}_1$ component being the most energetic.

Instantaneous spanwise vorticity $\overline{\omega}_3$ and streamwise vorticity $\overline{\omega}_1$ contours with the step height and inflow velocity in typical $x_1 - x_2$ and $x_2 - x_3$ planes are shown in Figure 21.7.2.5 for runs $A2$, $B1$, $B2$, and C_1. The shear layer separating from the step rolls up into coherent $\overline{\omega}_3$ vortices due to the shear layer instability. They undergo helical
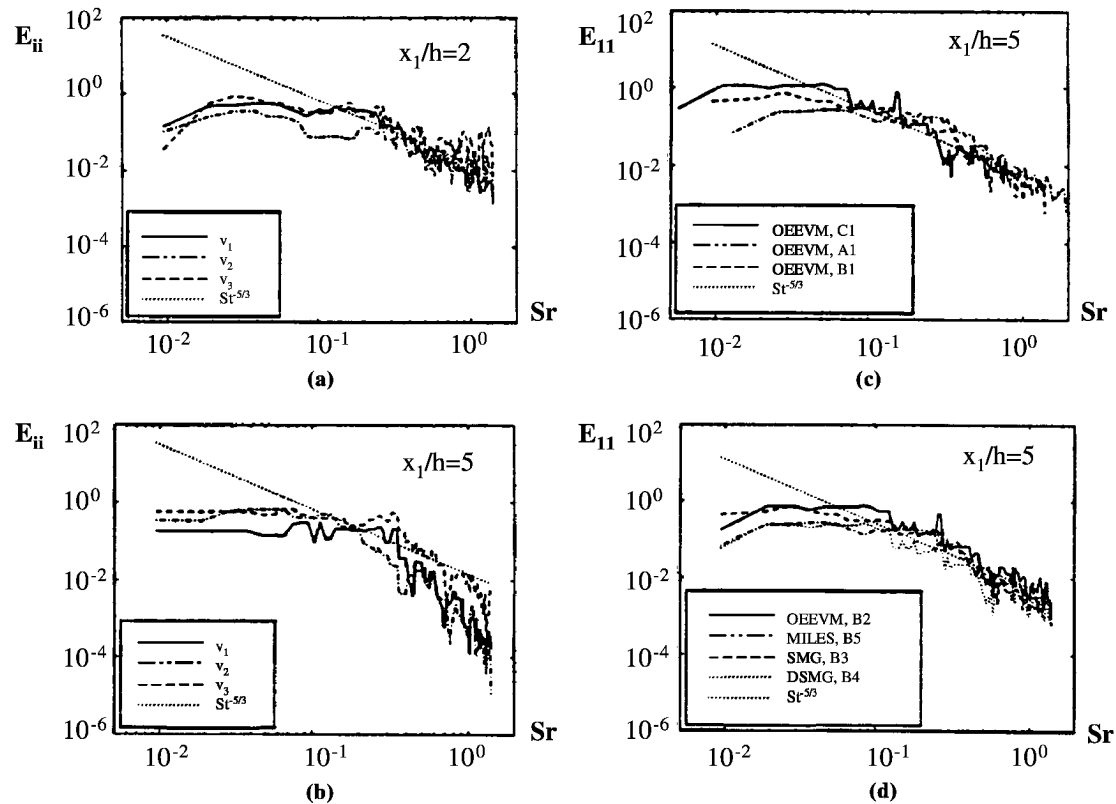
Figure 21.7.2.4 Energy spectra downstream of the step [Fureby, 1999]. **(a)** Component-based spectra for case B2 at $x_1/h = 2$. **(b)** Component-based spectra for case B2 at $x_1/h = 5$. **(c)** $\bar{v}_1$-based spectra for different Reynolds numbers at $x_1/h = 5$. **(d)** $\bar{v}_1$-based spectra for different LES models at $x_1/h = 5$.
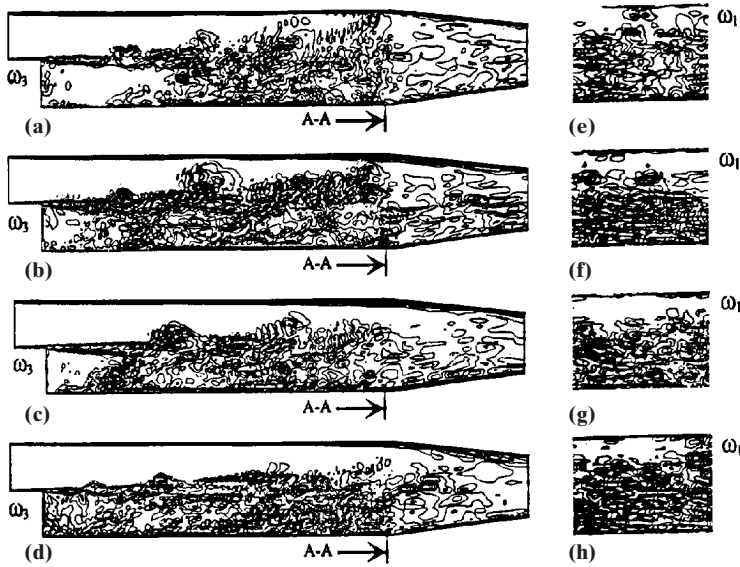
Figure 21.7.2.5 Instantaneous spanwise $\overline{\omega}_3$ and streamwise vorticity $\overline{\omega}_1$ contours normalized with the step height and inflow velocity in typical $x1 - x2$ and $x2 - x3$ planes: (a) $\overline{\omega}_3$ run A2, (b) $\overline{\omega}_3$ run B1, (c) $\overline{\omega}_3$ run B2, (d) $\overline{\omega}_3$ run C1, (e) $\overline{\omega}_1$ run A2, (f) $\overline{\omega}_1$ run B1, (g) $\overline{\omega}_1$ run B2, (h) $\overline{\omega}_1$ run C1 [Fureby, 1999].

pairing as they are advected downstream to endure vortex stretching effects due to the three-dimensionality of the flow.

(2) Compressible Flows

The large eddy simulations for compressible flows have been studied by many investigators. Among them are Speziale et al. [1988], Moin et al. [1991], Erlebacher et al. [1992], Spyropouros and Braisdell [1995], and Ducros et al. [1999].

The LES applications to compressible flows require higher order upwinding approximations of variables, particularly for shock wave/turbulence interactions. TVD or ENO schemes for FDM in Chapter 6 and stabilized FEM schemes in Chapter 13 may be used. Here we briefly describe the work of Ducros et al. [1999] on LES for shock/turbulence interactions.

In this work, a second order finite volume central scheme with FDM is used together with the artificial viscosity of Jameson et al. [1981] as shown in Section 6.6.1 and the filtered structure function (FSF) model [Metais and Lesieur, 1992] (see Section 21.4.3). Here a sensor (limiter) for triggering artificial dissipation is developed to perform LES of the shock/turbulent interaction by multiplying the standard limiter Ψ as given in (6.6.2) by the local function Φ defined as

$$\Phi = \frac{(\nabla \cdot \mathbf{v})^2}{(\nabla \cdot \mathbf{v})^2 + \omega^2 + \varepsilon} \tag{21.7.2.1}$$

where ω is the resolved vorticity and $\varepsilon = 10^{-30}$ is a positive small number so that this function varies between 0 for weakly compressible regions to about 1 in shock regions.
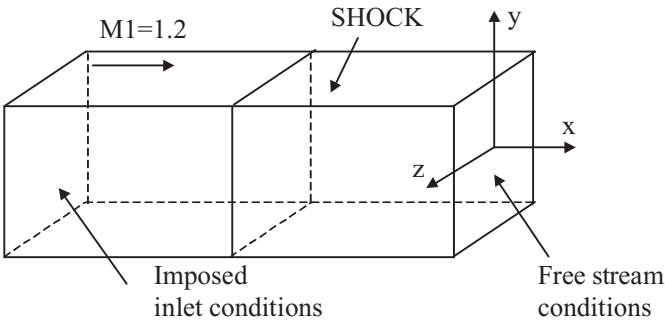
Figure 21.7.2.6   Schematic diagram of the computational domain for simulations ST-1 to ST-5. Periodic conditions are applied in the *y*- and *z*-directions [Ducros et al., 1999].

Thus, the artificial viscosity takes the form modified from that in (6.6.1) as

$$\varepsilon_{i+1/2}^{(2)} = k^{(2)} R_{i+1/2} \Psi_{i+1/2} \Phi_{i+1/2} \tag{21.7.2.2}$$

with

$$\Psi_{i+1/2} \Phi_{i+1/2} = \max(\Psi_i \Phi_i, \Psi_{i+1} \Phi_{i+1}) \tag{21.7.2.3}$$

The geometric configuration for the analysis is shown in Figure 21.7.2.6. The mean flow is in the *x*-direction, with the periodic boundary conditions applied in the *y*- and *z*-directions. Table 21.7.2.2 shows the various test cases, ST-1 through ST-5, with Ψ and $\Phi\Psi$ indicating the unmodified and modified versions, respectively. Figure 21.7.2.7 shows the distributions of the mean streamwise velocity, pressure, and Mach number. Note that the refined mesh gives a closer Rankine-Hugoniot jump condition.

Figure 21.7.2.8a,b shows the evolution of the normalized turbulent kinetic energy and turbulent Mach number for some simulations of Table 21.7.2.2. It is interesting to note that only the modified limiter $\Phi\Psi$ predicts a correct decay of turbulent kinetic energy for the preshock region, whereas the standard limiter [Jameson et al., 1981] exhibits a spurious dissipation (ST-1 and ST-3). As observed in Lee et al. [1993] and Lee et al. [1997], the isotropic flow becomes axisymmetric through the shock. This is

Table 21.7.2.2   Parameters of Simulations for the Three-Dimensional Shock/Turbulence Interaction

Simulation	(n_x, n_y, n_z)	Grid	K^2	k^3	Limiter
ST-1	$64 \times 32 \times 32$	Isotropic	1.5	0.02	ψ
ST-2	$64 \times 32 \times 32$	Isotropic	1.5	0	$\phi\psi$
ST-3	$262 \times 32 \times 32$	Locally refined	1.5	0.02	ψ
ST-4	$262 \times 32 \times 32$	Locally refined	1.5	0	$\phi\psi$
ST-5	$156 \times 32 \times 32$	Locally refined	1.5	0	$\phi\psi$

Note: The resolutions are referred to as resolution 1 (respectively, 2, 3) for $64 \times 32 \times 32$ (respectively, $262 \times 32 \times 32$ and $156 \times 32 \times 32$).
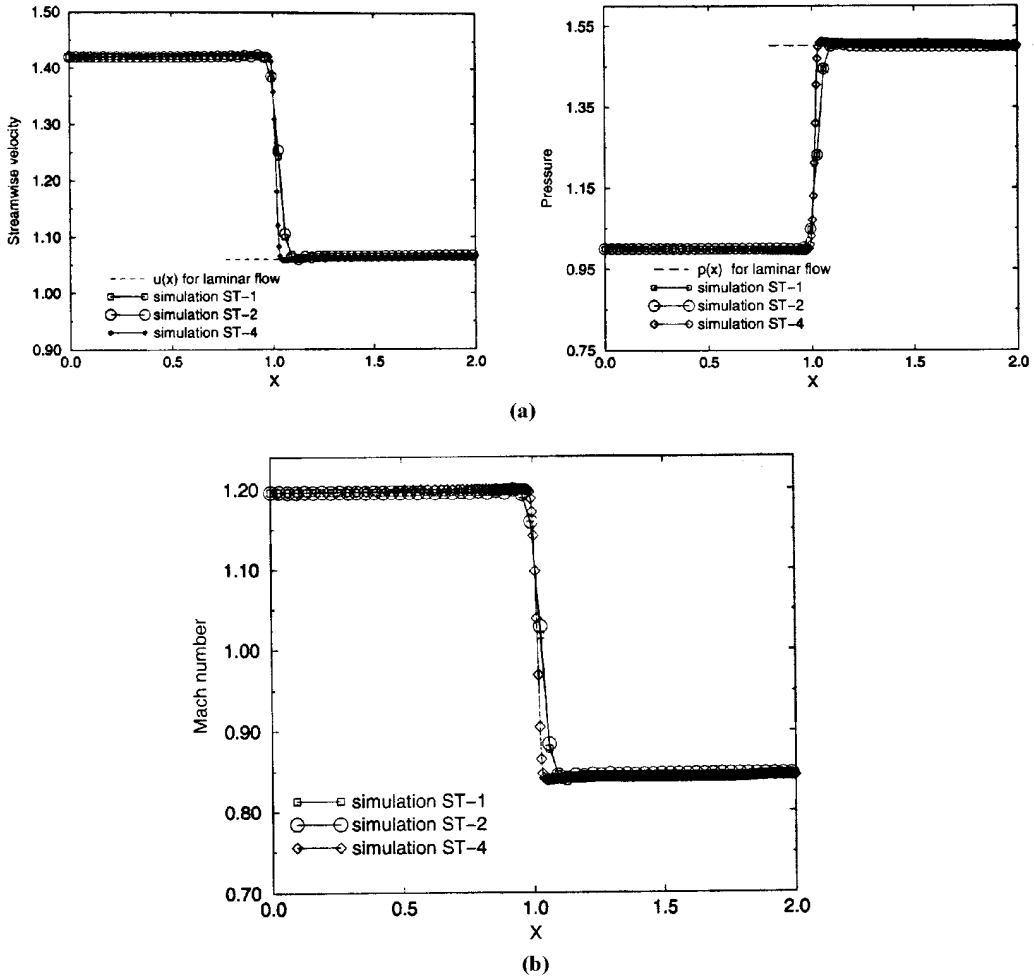Source: [Ducros et al., 1999]. Reprinted with permission from Academic Press.

(a)

(b)

Figure 21.7.2.7 The x distribution of mean streamwise velocity, pressure, and Mach number [Ducros et al., 1999]. **(a)** X distribution of mean steamwise velocity $\overline{u}$ (top) and mean pressure $\overline{p}$ (bottom) accross the shock wave for simulations ST-1, ST-2, and ST-4; dashed lines denote the laminar values satisfying Rankine-Hugoniot jump conditions. **(b)** The x distribution of mean Mach number for simulations ST-1, ST-2, and ST-4 with the same legend as the previous figure.

shown in Figure 21.7.2.8c by the streamwise distribution of the Reynolds stresses (ST-2 and ST-4).

The streamwise and spanwise distributions of normalized vorticity fluctuations are displayed in Figure 21.7.2.9. Note that the cases of standard limiter (ST-1 and ST-3) leads to a spurious decay of vorticity, whereas this non-physical behavior is corrected by means of the modified limiter (ST-2, ST-4, ST-5).

Figure 21.7.2.10a shows a cut of instantaneous streamwise and spanwise components of vorticity for ST-1. No change in size and intensity of the scales for both components is visible, although the size of the smallest scales is larger than the width of the shock. The same variables for ST-4 are shown in Figure 21.7.2.10b. Here, the x-component
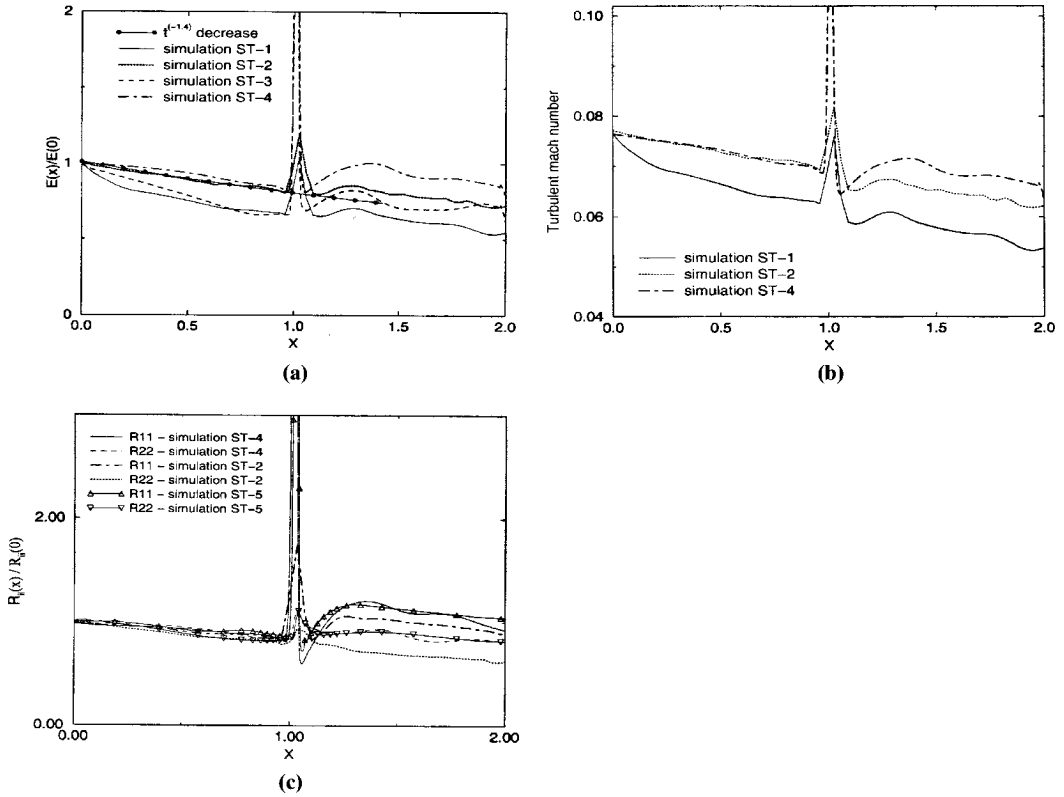
Figure 21.7.2.8 The x distribution of normalized turbulence kinetic energy, turbulent kinetic Mach number, and normalized Reynolds stresses [Ducros et al., 1999]. (a) The x distribution of normalized turbulence kinetic energy $\overline{E(x)}/\overline{E(0)}$ for simulations ST-1-4. (b) The x distribution of turbulence Mach number $\overline{M}_t$ for simulations ST-1, 2, 4. (c) The x distribution of normalized Reynolds stress $R_{ii}(x)/R_{ii}(0)$ for stimulations ST-2, 4, 5.
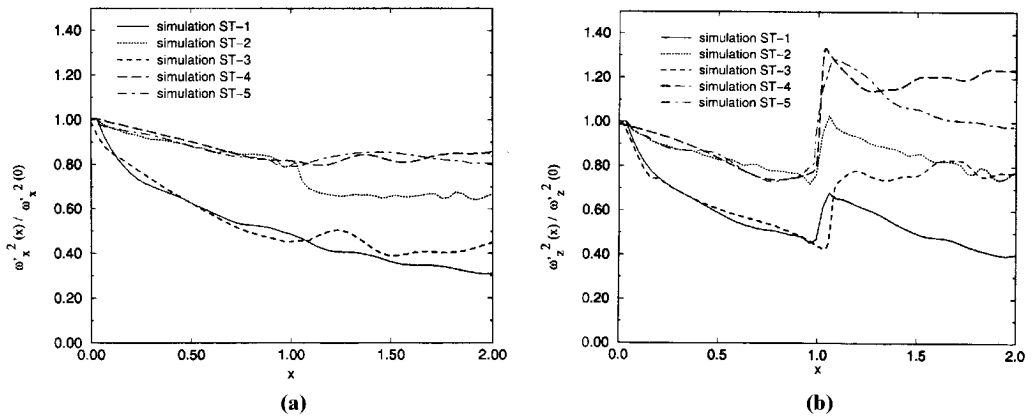

Figure 21.7.2.9 The x distribution of normalized fluctuation vorticity components [Ducros et al., 1999]. (a) The x distribution of normalized fluctuations vorticity component $\overline{\omega_x^2}(x)/\overline{\omega_x^2}(0)$ for simulations ST-1-5. (b) The x distribution of normalized fluctuations vorticity component $\overline{\omega_z^2}(x)/\overline{\omega_z^2}(0)$ for simulations ST-1-5.
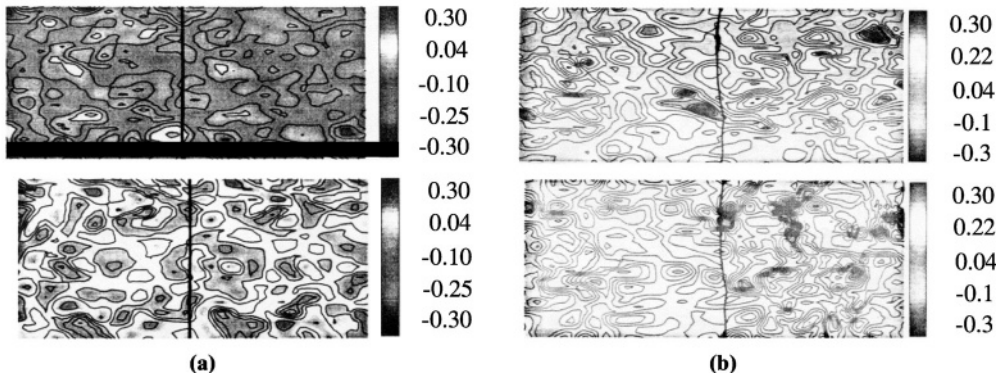
Figure 21.7.2.10 Instantaneous cut of the streamwise vorticity components [Ducros et al., 1999]. **(a)** Instantaneous cut of the streamwise ω_x, (top) and of the transverse to ω_z (bottom) vorticity field for simulation ST-1. Isopressure lines show the instantaneous position of the shock. The mean flow goes from left to right. **(b)** Instantaneous cut of the streamwise ω_x, (top) and of the transverse to ω_z (bottom) vorticity field for simulation ST-4. Isopressure lines show the instantaneous position of the shock. The mean flow goes from left to right.

undergoes a little change in intensity, while the intensity of the z-component increases through the shock and some structures of smaller scales appear in the post-shock region.

21.7.3 DIRECT NUMERICAL SIMULATION (DNS) FOR COMPRESSIBLE FLOWS

The research on DNS was primarily concentrated on incompressible flows [Kim et al., 1987; Spalart, 1988; Moser and Moin, 1984, among others]. Recently, DNS calculations have been extended to compressible flows [Pruett and Zang, 1992; Rai and Moin, 1993; Huang et al., 1995, among others]. From the numerical viewpoint, the direct numerical simulation is much more difficult in compressible flows dealing with higher Reynolds numbers and higher Mach numbers. As an example, we present here the work of Rai and Moin [1993].

In this example, the analysis is carried out using the temporally fully implicit and fifth order accurate spatial discretization with FDM for the primitive flow variables as shown in Section 6.6.2. Also, the inlet boundary conditions include the perturbation velocity components given by the Fourier series representation for the 3-D channel flow.

The geometry with a zonal grid system and the two grid options (A,B) are presented in Figure 21.7.3.1a,b. The computed power spectrum, skin friction, and mean velocity profiles are shown in Figure 21.7.3.2, whereas turbulence intensities and Reynolds stress distributions are presented in Figure 21.7.3.3. The results appear to be qualitatively in agreement with experimental data.

Figure 21.7.3.4a represents spanwise vorticity contours in an (x, y) plane at different times in the transition region with the y-direction expanded by a factor of 10 and the letter "d" on the ordinate indicating the laminar boundary layer thickness at $Re_x = 2.5 \times 10^5$. This figure shows the rollup of its tip into a spanwise vortex. Streamwise vorticity contours at $y^+ = 34.5$ are presented in Figure 21.7.3.4b. The letter "s" on the ordinate denotes the dimension of the computational region in the z-direction. Here.
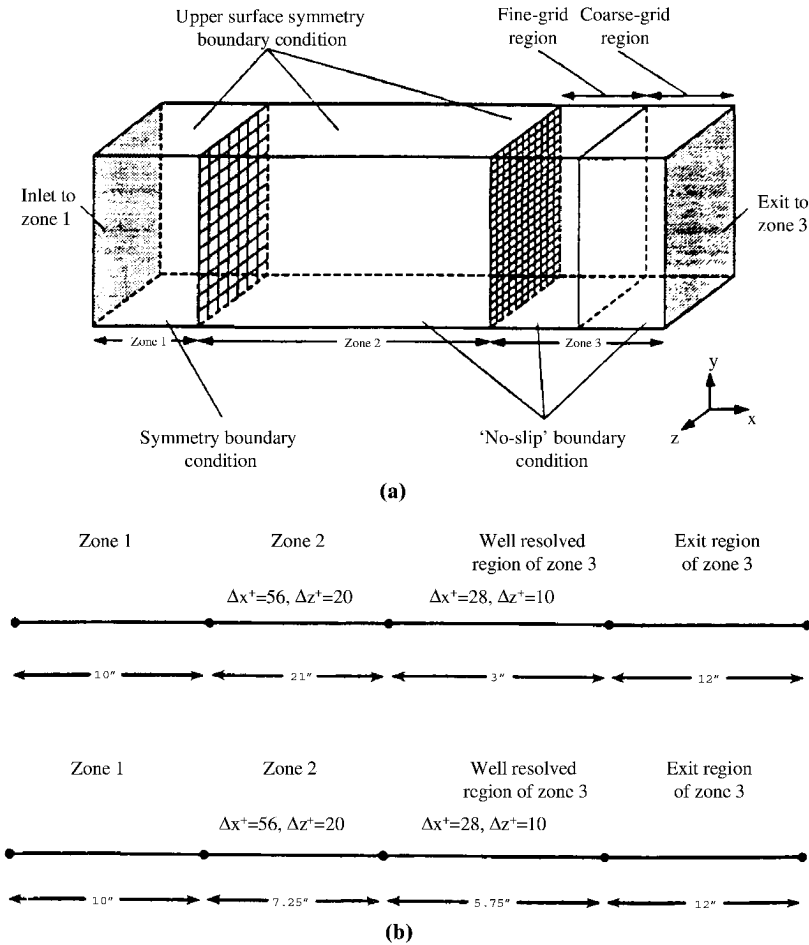
Figure 21.7.3.1 The geometry of 3-D duct and zonal grid system [Rai and Moin, 1993]. **(a)** Schematic of computational region (not to scale). **(b)** Zonal configurations used in grids A and B.

it is seen that the transition boundary is marked by the appearance of counter-rotating vortex pairs in the region $Re_x \leq 4.0 \times 10^5$. Figure 21.7.3.4c shows crossflow velocity vectors in a (y, z) plane cutting through the largest pair of vortices. The letter "d" on the ordinate represents the laminar boundary layer thickness at $Re_x = 4.0 \times 10^5$. The cross sectional structure of this pair of vortices is clearly seen in this figure. Further details are given in Rai and Moin [1993].

Some recent contributions in DNS include Pointsot and Lele [1992], Pruett and Zang [1992], Choi et al. [1993], Lee et al. [1993], Huser and Biringen [1993], Huang et al [1995]. Pruett et al [1995], Mittal and Balachandar [1996], and Guo et al. [1996], among others. In all cases, the main features in DNS are that higher order accurate computational methods must be used with refined mesh, and thus the computer cost will be very excessive.
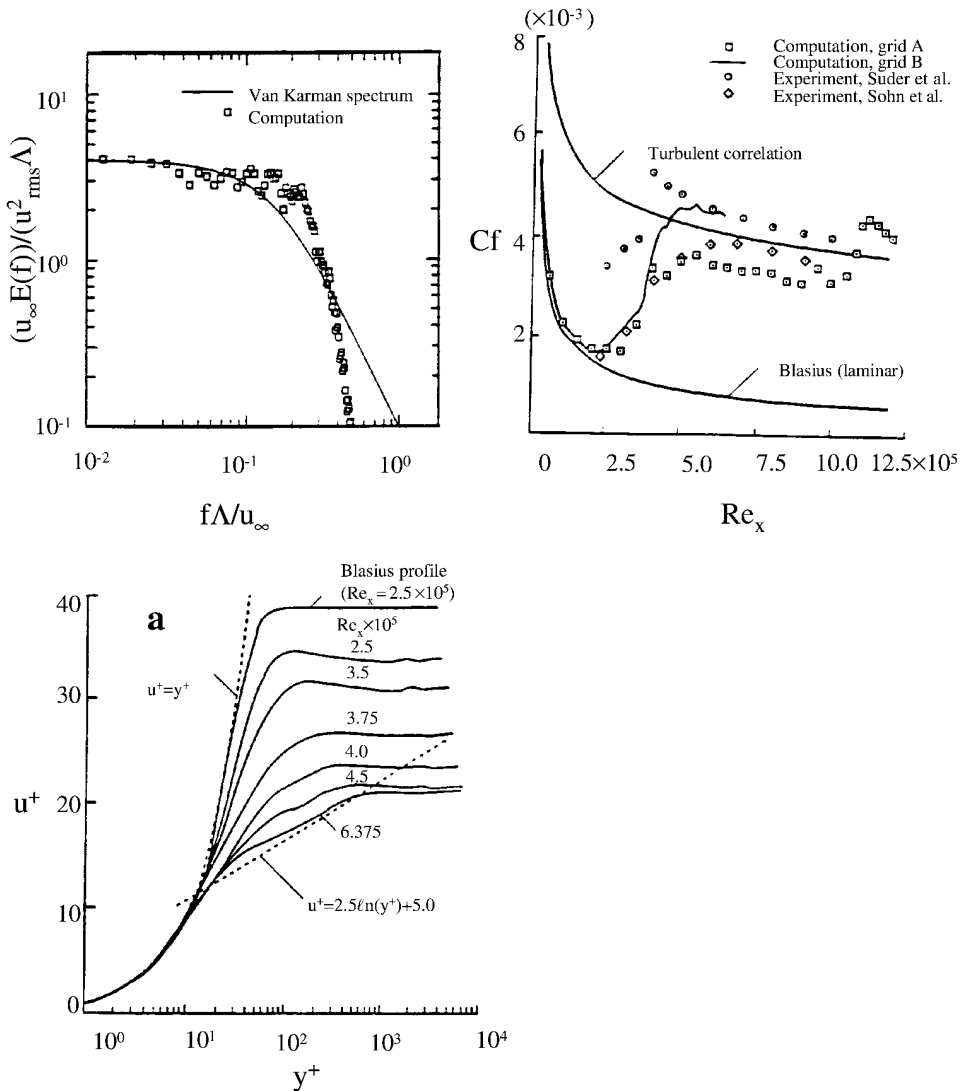
Figure 21.7.3.2   Power spectrum, skin friction, and mean velocity profiles [Rai and Moin, 1993]. Reprinted with permission from Academic Press.

21.8   SUMMARY

In this chapter, we have provided a brief review of the current state of the art on turbulence, including not only the theory of turbulence but also the examples of computations. Turbulence models with Reynolds averaged Navier-Stokes equations (RANS), large eddy simulation (LES), and direct numerical simulation (DNS) are covered.

Turbulence models include zero-equation models, one-equation models, two-equation models, second order closure models (Reynolds stress models), algebraic Reynolds stress models, and models with compressibility effects. Their advantages and disadvantages are noted.

Although the turbulence model approaches are still used in practice, there is a trend toward favoring LES for more accuracy, in which large scales are calculated and only the
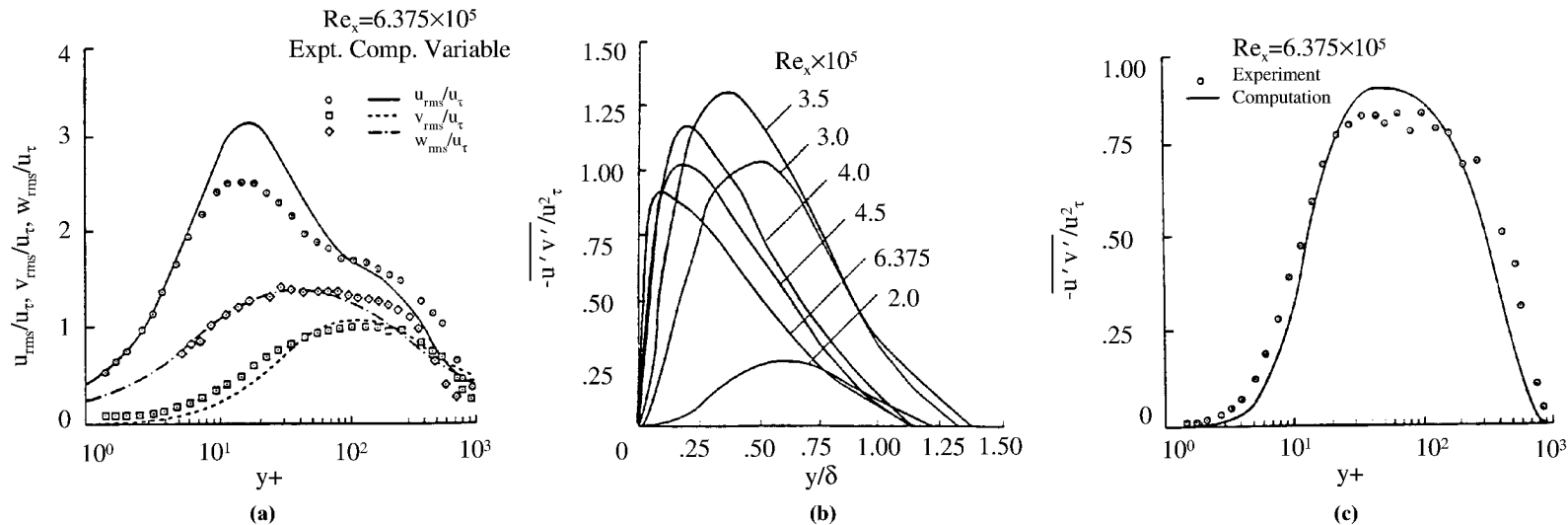
Figure 21.7.3.3 Turbulence intensities and Reynolds stress distributions [Rai and Moin, 1993]. (a) Turbulence intensities at streamwise location $\mathrm{Re}_x = 6.375 \times 10^5$, normalized by wall-shear velocity and plotted in wall coordinates. (b) Reynolds shear-stress distributions at various streamwise locations, normalized by the square of the wall-shear velocity. (c) Reynolds shear-stress distributions at the streamwise location $\mathrm{Re}_x = 6.375 \times 10^5$, normalized by the square of the wall-shear velocity and plotted in wall coordinates. Reprinted with permission from Academic Press.
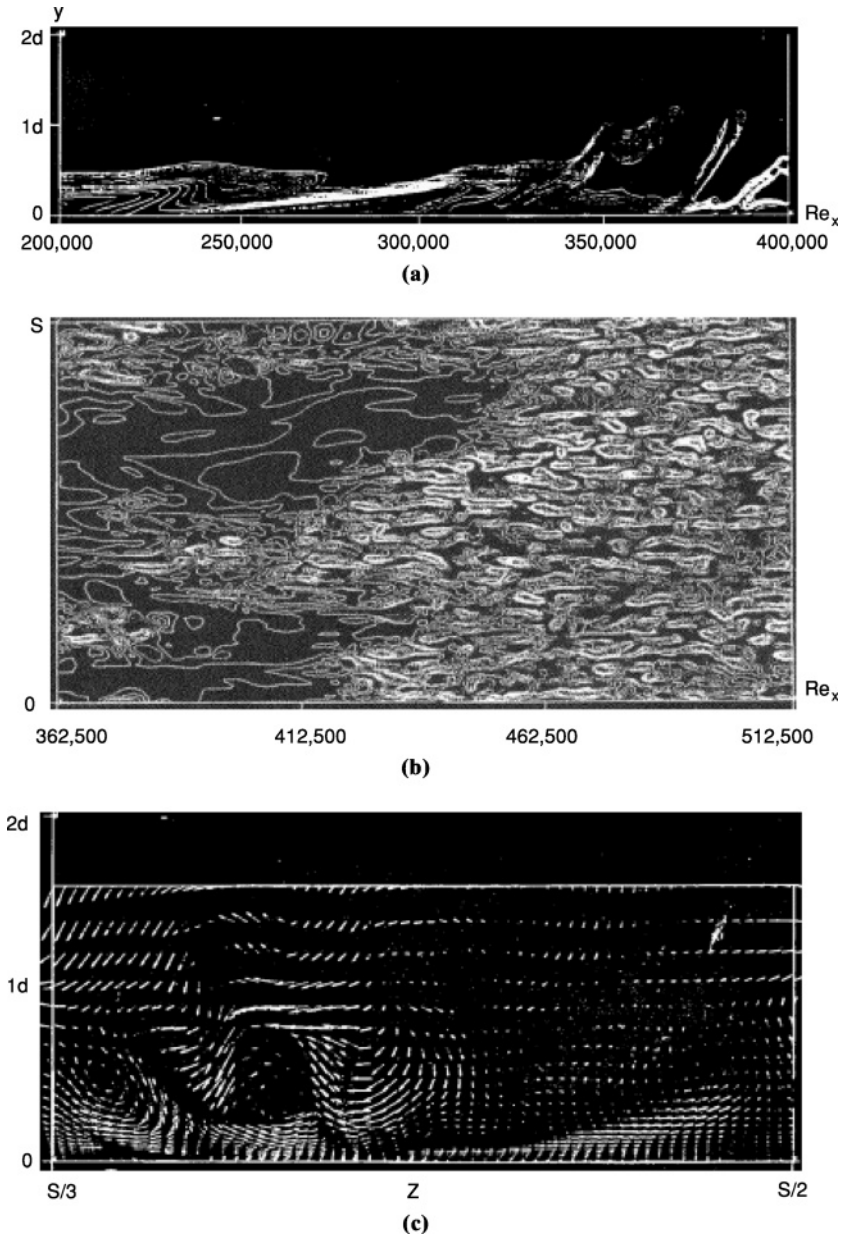
Figure 21.7.3.4 Spanwise and streamwise vorticity contours and crossflow velocity vectors [Rai and Moin, 1993]. **(a)** Spanwise vorticity contours in (x, y) plane, $2.5 \times 10^5 \leq \mathrm{Re}_x \leq 4.0 \times 10^5$, $t = 51.25\delta^*/u_\infty$. **(b)** Streamwise vorticity contours in (x, y) plane, $y^+ = 34.5$, $3.6 \times 10^5 \leq \mathrm{Re}_x \leq 5.1 \times 10^5$, $0 \leq Z \leq 5$. **(c)** Crossflow velocity vectors at the streamwise location $\mathrm{Re}_x = 384,375$. Reprinted with permission from Academic Press.

small scales are modeled. However, the small scale modeling is still in need of further research for high-speed compressible flows and reactive flows.

Our ultimate goal is then the DNS in which no modeling is required. Unfortunately, the state of the art on DNS is far from practical applications due to demands in unavailable computer resources. If and when DNS becomes a reality, then our concern is the most accurate numerical simulation approaches from those introduced in Parts Two and Three. This will be the focus of our research in the future. In this vein, the FDV theory introduced in Sections 6.5 and 13.6 will be particularly useful in resolving turbulence microscales as accurately as possible. Some examples of FDV applications with K–ε turbulence models for combustion are presented in Section 22.6.2.

REFERENCES

Baldwin, B. S. and Lomax, H. [1978]. Thin-layer approximation and algebraic model for separated turbulent flows. AIAA paper 78-257.

Bardina, J., Ferziger, J. H., and Reynolds, W. C. [1980]. Improved subgrid-scale models for large eddy simulation. AIAA paper, 80-1357.

Cebeci, T. and Smith, A. M. O. [1974]: Analysis of turbulent boundary layer. In *Appl. Math. Mech., 15*, Academic Press.

Choi, H., Moin, P., and Kim, J. [1993]. Direct numerical simulation of turbulent flow over rivets. *J. Fluid Mech.* 255, 503–39.

Comte, P. [1994]. Structure-function based models for compressible transitional shear flows. *ERCOFTAC Bull.*, 22, 9–14.

Comte, P. and Lesieur, M. [1989]. Coherent structure of mixing layers in large eddy-simulation in topological fluid dynamics. In H. K. Moffatt (ed.). *Topological Fluid Dynamics.* New York: Cambridge University Press, 360–80.

Ducros, F., Ferrand, V., Nicoud, F., Weber, C., Darracq, D., Gacherieu, C., and Poinsot, T. [1999]. Large-eddy simulation of the shock/turbulence interaction. *J. Comp. Phys.*, 152, 517–49.

Dumuren, A. O. [1991]. Calculation of turbulent-driven secondary motion in ducts with arbitrary cross section. *AIAA J.*, 29, 4, 531–37.

Erlebacher, G., Hussaini, M. Y., Speziale, C. G., and Zang, T. A. [1992]. Towards the large eddy simulation of compressible turbulent flows. *J. Fl. Mech.*, 238, 155–85.

Fasel, H. F., Rist, U., and Konzelmann, U. [1990]. Numerical investigation of the three-dimensional development in boundary layer transition. *AIAA J.*, 28, 1, 29–37.

Fureby, C. [1999]. Large eddy simulation of rearward-facing step flow. *AIAA J.*, 37, 11, 1401–10.

Gao, F. and O'Bien, E. E. [1991]. Direct numerical simulation of reacting flows in homogeneous turbulence. *AIChE J.*, 37, 1459–70.

Gatski, T. B. and Speziale, C. G. [1992]. On explicit algebraic stress models for complex turbulent flows. ICASE Report No. 92-58, Univ. Space Research Assoc., Hampton, VA.

Germano, M. [1992]. Turbulence: the filtering approach. *J. Fl. Mech.*, 238, 325–36.

Germano, M., Piomelli, U., Moin, P., and Cabot, W. H. [1991]. A dynamic subgrid-scale eddy viscosity model. *Phys. Fl.*, A, 3, 1760–65.

Girimaji, S. S. [1995]. Fully explicit and self-consistent algebraic Reynolds stress model, ICASE Report No. 95-82, NASA Langley Research Center.

Guo, Y. Kleiser, L., and Adams, N. A. [1996]. Comparison of temporal and spatial direct numerical simulation of compressible boundary layer transition. *AIAA J.*, 34, 4, 683–90.

Hanine, F. and Kourta, A. [1991]. Performance of turbulence models to predict supersonic boundary layer flows. *Comp. Meth. Appl. Mech. Eng.*, 89, 221–35.

Huang, P. G., Bradshaw. P., and Coakley. T. J. [1992]. Assessment of Closure Coefficients for Compressible-Flow Turbulence Models, NASA TM-103882.

Huang, P. G., Coleman, G. N., and Bradshaw, P. [1995]. Compressible turbulent channel flows: DNS results and modeling. *J. Fluid Mech.*, 305, 185–218.

Huser, A. and Biringen, S. [1993]. Direct numerical simulation of turbulent flow in a square duct. *J. Fluid Mech.*, 257, 65–95.

Jameson, A., Schmidt, W., Turkel, E. [1981]. Numerical solutions of the Euler equations by finite volume methods using Runge-Kutta time stepping. AIAA paper, 81-1250.

Kim, J., Kline, S. J., and Johnston, J. P. [1980]. Investigation of a reattaching turbulent shear layer: Flow over a backward-facing step. *ASME J. Fl. Eng.*, 102, 302–8.

Kim, J., Moin, P., and Moser, R. [1987]. Turbulence statistics in fully developed channel flow at low Reynolds number. *J. Fl. Mech.*, 177, 133–66.

Knight, D., Zhou, G., Okong'o, N., and Shukla, V. [1998]. Compressible large eddy simulation using unstructured grids. AIAA paper, 98-0535.

Kolmogorov, A. N. [1941]. Local structure of turbulence in incompressible viscous fluid for very large Reynolds number. *Doklady AN. SSR*, 30, 299–303.

———[1942]: Equations of turbulent motion of an incompressible fluid. *Izvestia Academy of Sciences, USSR, Physics*, 6, 1, 56–58.

Launder, B. E. (ed.). [1992]. *Fifth Biennial Colloquium on Computational Fluid Dynamics*. Manchester Institute of Science and Technology, England.

Launder B. E., Reece G. J., and Rodi W. [1975]. Progress in the development of Reynolds stress turbulent closure. *J. Fl. Mech.*, 68, 537–66.

Launder, B. E. and Spalding, B. [1972]. *Mathematical Models of Turbulence*. New York: Academic Press.

Lee, S., Lele, S. K., and Moin, P. [1993]. Direct numerical simulation of isotropic turbulence interacting with a weak shock wave. *J. Fl. Mech.*, 251, 533–62.

Lesieur, M. [1997]. *Turbulence in Fluids*. London: Kluwer Academic Publishers.

Lesieur, M and Metais, O. [1996]. New trends in large eddy simulation of turbulence. *Ann. Rev. Fl. Mech.*, 28, 45–63.

Lilly, D. K. [1966]. On the application of the eddy viscosity concept in the inertial subrange of turbulence. NCAR-123, National Center for Atmospheric Research, Boulder, CO.

———[1992]. A proposed modification of the Germano subgrid-scale closure methods. *Phys. Fl., A*, 4, 633–35.

Lumley, J. L. [1978]. Computational modeling of turbulent flows, *Adv. Appl. Mech.*, 18, 123–76.

Meneveau, C. and Lund, T. S. [1997]. The dynamic Smagorinsky model and scalar-dependent coefficients in the viscous range of turbulence. *Phys. Fl.*, 9, 3932–34.

Metais, O. and Lesieur, M. [1992]. Spectral large eddy simulations of isotropic and stably stratified turbulence. *J. Fl. Mech.*, 239, 157–94.

Mittal, R. and Balachandar, S. [1996]. Direct numerical simulation of flow past elliptic cylinders. *J. Comp. Phys.*, 124, 351–67.

Moin, P., Squires, K., Cabot, W., and Lee, S. [1991]. A dynamic subgrid-scale model for compressible turbulence and scalar transport. *Phys. Fl.*, 3, 2746–57.

Moser, R. D. and Moin, P. [1984]. Direct numerical simulation of curved turbulent channel flow. NASA TM-85974.

Normand, X. and Lesieur, M. [1992]. Direct and large-eddy simulation of laminar break-down in high-speed axisymmetric boundary layers. *Theor. Comp. Fl. Dyn.*, 3, 231–52.

Pierce, C. D. and Moin, P. [1999]. A dynamic model for subgrid-scale variance and dissipation rate of a conserved scalar. *Phys. Fl.*, 10, 3041–44.

Pitz, R. W. and Daily, J. W. [1981]. Experimental study of combustion: the turbulent structure of a reacting shear layer formed at a rearward facing step. NASA CR 165427.

Poinsot, T. J. and Lele, S. K. [1992]. Boundary conditions for direct simulations of compressible viscous flows. *J. Comp. Phys.*, 101, 104–29.

Prandtl, L. [1925]. Uber die ausgebildete turbulenz. *Z. Angew. Math. Mech.*, 136–39.

Pruett, C. D. and Zang, T. A. [1992]. Direct numerical simulation of laminar breakdown in high-speed, axisymmetric boundary layers. *Tjeoret. Comp. Fl. Dyn.*, 3, 345–67.

Pruett, C. D., Zang, T. A., Chang, C. L., and Carpenter, M. H. [1995]. Spatial direct numerical simulation of high-speed boundary layer flows. Part I: Algorithmic considerations and validation. *Theor. Comp. Fl. Dyn.* 7, 49–76.

Rai, M. M. and Moin, P. [1993]. Direct numerical simulation of transition and turbulence in a spatially evolving boundary layer. *J. Comp. Phys.*, 109, 169–92.

Rodi, W. [1976]. A new algebraic relation for calculating Reynolds stresses. *ZAMM*, 56, 219.

Rotta, J. C. [1951]. Statisische theorie nichthomogener turbulenz. *Zeitschrift fur Physik*, 129, 547–72.

Sarker, S., Erlebacher, G., Hussaini, M. Y., and Kreiss, H. O. [1989]. The analysis and modeling of dilatational terms in compressible turbulence, ICAS Report 89-79. Hampton VA: Univ. Space Research Assoc.

Smagorinsky, J. [1963]. General circulation experiments with the primitive equations, I. The basic experiment. *Mon. Weather Rev.*, 91, 99–164.

So, R.M.C. and Melloe, G. L. [1978]. Turbulent boundary layers with large streamline curvature effects. *ZAMP*, 29, 54–74.

Spalart, P. R. [1988]. Direct simulation of a turbulent boundary layer up to Re = 1410. *J. Fl. Mech.*, 187, 61–98.

Spalart, P. R. and Yang, K. S. [1987]. *J. Fl. Mech.*, 178, 345–58.

Spalding, D. B. [1972]. A novel finite difference formulation for differential equations involving both first and second derivatives. *Int. J. Num. Meth. Eng.*, 4, 551–59.

Speziale, C. G. [1987]. On non-linear $K–\ell$ and $K–\varepsilon$ model of turbulence. *J. Fl. Mech.*, 178, 459–75.

Speziale, C. G., Erlebacher, G., Zang, T. A., and Hussaini, M. Y. [1988]. The subgrid-scale modeling of compressible turbulence. *Phys. Fl.*, 31, 940.

Speziale, C. G., Sarker, S., and Gatski, T. B. [1991]. Modeling of the pressure-strain correlation of turbulence, *J. Fl. Mech.*, 227, 245–72.

Speziale, C. G., Zang, T. A., and Hussaini, M. Y. [1988]. The subgrid scale modeling of compressible turbulence. *Phys. Fl.*, 31, 940–42.

Spyropoulos, E. T. and Blaisdell, G. A. [1995]. Evaluation of the dynamic subgrid-scale model for large eddy simulation of compressible turbulent flows. AIAA paper, 95-0355.

Squires, K. D. [1991]. Dynamic subgrid-scale modeling of compressible turbulence. *Annual Research Briefs*, Center for Turbulence Research, Stanford University, 207–23.

Thangam, S. and Hur, N. [1991]. A highly resolved numerical study of turbulent separated flow past a backward-facing step. *Int. J. Eng. Sci.*, 29, 5, 607–15.

Thangam, S. and Speziale, C. G. [1992]. Turbulent flow past a backward-facing step: a critical evaluation of two-equation models. *AIAA J.*, 30, 5, 1314–20.

Van Driest, E. R. [1956]. On turbulent flow near a wall. *J. Aero. Sci.*, 23, 1007–11.

Vreman, B., Geurts, B., and Kuerten, H. [1995]. Subgrid-modeling in LES of compressible flows. *Appl. Sci. Res.*, 54, 191–203.

Wilcox, D. C. [1988]. Multiscale model for turbulent Flows. *AIAA J.*, 26, 11, 1311–20.

———[1989]. Wall matching, a rational alternative to wall functions. AIAA paper, 89-611.

———[1992a]. Dilatation-dissipation corrections for advanced turbulence models, *AIAA J.*, 30, 11, 2639–46.

———[1992b]. *Turbulence Modeling for CFD*, DCW Industries, Inc., La Canada, CA.

Yoshzawa, A. [1986]. Statistical theory for compressible turbulent shear flows with the application to subgrid modeling. *Phys. Fl. A*, 29, 2152–64.

Zang, Y., Street, R. L., and Koseff, J. R. [1993]. A dynamic mixed subgrid-scale and its application to turbulenct recirculating flows. *Phys. Fl.* A, 5, 3186–96.

Zeman, O. [1990]. Dilatation dissipation: The concept and application in modeling compressible mixing layers. *Phys. Fl.* A, 2, no. 2, 178–88.